

## PHYSICAL PROPERTIES OF THE SOLAR MAGNETIC PHOTOSPHERE UNDER THE MISMA HYPOTHESIS III: SUNSPOT AT DISK CENTER

J. SÁNCHEZ ALMEIDA

Instituto de Astrofísica de Canarias, E-38205 La Laguna, Tenerife, Spain

@/scratch/asp/95.10.15/text/ms.tex

### ABSTRACT

Small-scale fluctuations of magnetic field and velocity may be responsible for the Stokes asymmetries observed in all photospheric magnetic structures (the MISMA hypothesis). We support the hypothesis showing that atmospheres with optically-thin micro-structure reproduce the polarization of Fe I  $\lambda 6301.5$  Å and Fe I  $\lambda 6302.5$  Å observed in a sunspot. Ten thousand spectra were fitted by model MISMA with two magnetic components interleaved along the line-of-sight. Combining all the fits, we set up a semi-empirical model sunspot characterized by two components with very different magnetic field inclination. The major component, which contains most of the mass, is more vertical than the minor component. The field lines of the minor component are inclined below the horizontal plane throughout the penumbra. Magnetic field lines and mass flows are parallel, consequently, both upflows and downflows are present everywhere on the penumbra. Major and minor components have very different velocities (several hundred  $\text{m s}^{-1}$  for the major component versus  $10 \text{ km s}^{-1}$  for the minor component), but the mass transported per unit time is similar. The similarity between the vertical mass flow and the magnetic flux of the two components suggests that field lines emerging as major component may return to the photosphere as minor component. If so, the observed magnetic field strength difference between components leads to a siphon flow whose magnitude and direction agree with the inferred Evershed flow. Several tests support the internal consistency of the retrieved model sunspot. The magnetic field vector  $\mathbf{B}$  does not violate the  $\nabla \cdot \mathbf{B} = 0$  condition. The model sunspot reproduces the net circular polarization of the observed lines, plus the abnormal behavior of Fe I  $\lambda 15648$  Å. The use of only one magnetic component to interpret the spectra leads to inferring upflows in the inner penumbra and downflows in the outer penumbra, in agreement with previous findings.

*Subject headings:* line: profiles – polarization – methods: data analysis – Sun: magnetic fields – Sun: photosphere – sunspots

### 1. INTRODUCTION

Ubiquitous small-scale fluctuations of the magnetic field and the velocity may be responsible for the Stokes asymmetries<sup>1</sup> observed in all photospheric magnetic structures. If the spatial scale is small enough to be optically-thin, one has a very efficient source of line asymmetry. The existence of such gradients was conjectured by Sánchez Almeida et al. (1996), that coined the acronym MISMA to describe magnetic atmospheres having optically-thin irregularities (MISMA  $\equiv$  MICRO-STRUCTURED MAGNETIC ATMOSPHERE). If the conjecture turns out to be correct, we must understand the magnetic micro-structure for two fundamental reasons. First, many physical processes determining the magnetism at all scales take place at micro-scales (e.g., ohmic diffusion, advection, onset of instabilities, viscous stresses, etc.). Second, it plays a key role for the proper interpretation of the magnetic field measurements, which are prone to bias if the micro-structure is overlooked. (For a more elaborated discussion on these two reasons, see Sánchez Almeida 2001.)

This paper is the third of a series aimed at examining the conjecture in detail. We wanted to see (a) whether the observed asymmetries can be quantitatively explained by

MISMAs, and (b) what are the physical properties of the micro-structure. The first paper introduces an inversion code (IC) based on the MISMA concept. It is a (fairly) automatic algorithm to fit Stokes profiles using synthetic profiles formed in atmospheres with optically-thin micro-structure (Sánchez Almeida 1997, Paper I). As a test case, Paper I reproduces the asymmetries found in plage regions by Stenflo et al. (1984). The second paper describes the successful application of the IC to quiet Sun network and inter-network regions (Sánchez Almeida & Lites 2000, Paper II; see also Socas-Navarro & Sánchez Almeida 2002). The present paper extends the MISMA inversions to a sunspot, showing that the micro-structure is also able to cope with the Stokes asymmetries of sunspots.

The paper is organized as follows. The properties of the spectro-polarimetric data subject to analysis are summarized in § 2. Section 3 describes the constraints used to set up the model MISMA, the quality of the fits, and the procedure to assemble independent inversions from different pixels into a single coherent structure. The main results are set forth in the seven subsections of § 4. Specific aspects of the resulting model sunspot are examined in § 5 (magnetic flux conservation) and § 6 (mass conservation). Section § 7 explains the physical origin of the asymmetries from a radiative transfer point of view. Finally, § 8 comments on and summarizes the contents of the paper. The interpretation of these results in the context of the global penumbral magnetic field topology is deferred for a separate paper (Sánchez Almeida 2005). We have preferred to disconnect the fact that MISMA account for the Stokes asymmetries in sunspots (this work),

Electronic address: jos@iac.es

<sup>1</sup> We will use the standard notation for the Stokes parameters;  $I$  for the intensity,  $Q$  and  $U$  for the two independent types of linear polarization, and  $V$  for the circular polarization. The Stokes profiles are the function Stokes parameter versus wavelength for a particular spectral line. These Stokes profiles are expected to be symmetric or anti-symmetric when the line is formed in a homogeneous atmosphere, e.g., Unno (1956); Landi Degl'Innocenti (1992). Deviations from these symmetries are called Stokes asymmetries.

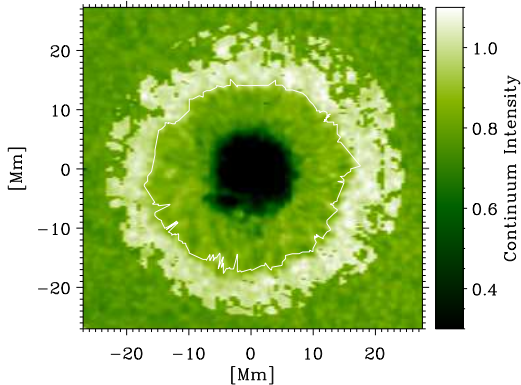


FIG. 1.— Continuum image of the inverted sunspot. Coordinates are given in Mm from the adopted sunspot center. Those pixels which have been inverted are artificially enhanced so that the sunspot and its surroundings stand out against a dark background of pixels without inversion. The white contour shows the border of the sunspot, and it is used for reference along the paper.

from the more speculative physical interpretation of the retrieved micro-structure. Even if the physical interpretation is eventually proved to be wrong, the micro-structure would still account for the asymmetries.

## 2. OBSERVATIONS AND DATA

The Stokes  $I$ ,  $Q$ ,  $U$  and  $V$  profiles analyzed in this work were obtained by Lites et al. (1998) with the Advanced Stokes Polarimeter (ASP; Elmore et al. 1992). They correspond to the sunspot in active region NOAA 7912 (Fig. 1) observed on 1995 October 15 when passing close to the solar disk center (S5, E9, cosine of heliocentric angle  $\mu = 0.96$ ). The region was scanned with a step-size of  $0''.75$  in the East-West direction, perpendicular to the slit. The pixel size along the spectrograph slit  $0''.37$ , is enough to sample a seeing close to (but better than)  $1''$ . The Field-Of-View (FOV) is set by the length of the slit, and the size of the scan, and it turns out to be  $85'' \times 135''$ . The ASP provides the polarization of Fe I  $\lambda 6301.5 \text{ \AA}$  and Fe I  $\lambda 6302.5 \text{ \AA}$  every  $12.8 \text{ m\AA}$ . An integration time per slit position of 10 sec affords a noise per spectral pixel better than  $10^{-3}$  times the continuum intensity. The spectra are corrected for instrumental polarization to a level below this noise (Skumanich et al. 1997). For further details on the observational setup and the target, refer to Lites et al. (1998). We use this rather old data set because its image quality was among the best ASP maps available when the work began in 1999.

The sunspot has negative polarity, i.e., the magnetic field lines are anti-parallel to the vertical direction at the umbral core. This fact introduces some minor complications in the interpretation of the sunspot magnetic field. They will be pointed out and clarified whenever they interfere with our argumentation.

The zero of the absolute velocity scale has been set using the Stokes  $V$  zero-crossing wavelengths in the plage around the sunspot. We use its mean position as null velocity. The same procedure was used in Paper II since observations have shown that the zero-crossing wavelengths of Stokes  $V$  profiles in plage are very close to the laboratory wavelengths of the lines (Solanki 1986; Martínez Pillet et al. 1997). The systematic error of our absolute velocities should be less than  $0.25 \text{ km s}^{-1}$ .

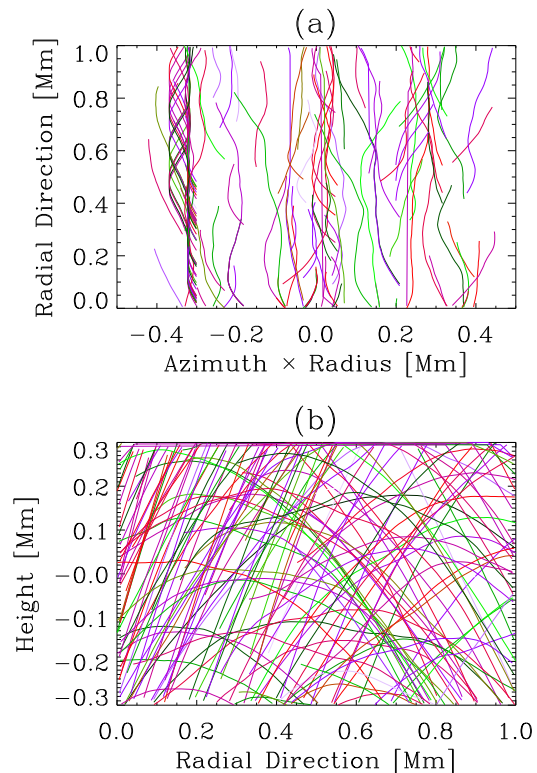
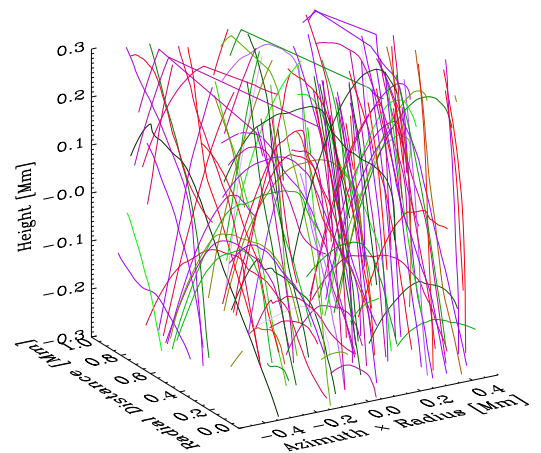


FIG. 2.— Top: cartoon with the kind of atmosphere used for inversion of sunspot Stokes profiles. It represents magnetic field lines in one resolution element. They overlap along any line-of-sight. (a) A view from above showing how the field lines are preferentially aligned along the sunspot radial direction. (b) A view from the side showing field lines with very different vertical inclinations.

## 3. INVERSION

### 3.1. MISMA scenario to represent umbrae and penumbrae

We employ the scenario proposed in Sánchez Almeida et al. (1996, § 3.1), which resembles a scaled-down version of the *uncombed fields* of Solanki & Montavon (1993). The atmosphere has two magnetic components which differ in velocity, inclination, as well as in many other physical parameters. It is a MISMA,

therefore, each line-of-sight crosses several different sub-structures (see the schematic in Fig. 2). Since we will use the Inversion Code (IC) by Sánchez Almeida (1997), these two components meet several physical requirements.

1. The temperature of the two magnetic components is the same at every geometrical height. We adopt this approach for consistency, since the radiative exchange among the optically-thin micro-structures of the MISMA should efficiently smooth temperatures in seconds (e.g., Spiegel 1957; Stix 1991)<sup>2</sup>.
2. In addition to the two magnetic components, there is a third non-magnetic component. It is introduced for technical reasons and plays no central role. As we will see (§ 4.1), the fraction of photospheric volume that it occupies within the sunspot is always marginal.
3. The three components are in lateral pressure balance at every geometrical height (i.e., they have the same total pressure, which is the sum of the gas pressure plus the magnetic pressure). This constraint and the assumption of hydrostatic equilibrium along field lines provide the full vertical stratification of magnetic field strengths from the strengths at one height. The field strengths of the different components are different.
4. The two magnetic components have different inclinations with respect to the vertical direction, but the same azimuth. Inclinations and azimuths do not vary with height in the atmosphere.
5. Only motions along magnetic field lines are allowed. The mass conservation along field lines determines the velocity stratification by setting the velocity at a given height.
6. Unpolarized stray light is accounted for. Dealing with stray light introduces three free parameters: the fraction of stray light, a global velocity, and a microturbulence. The thermodynamic stratification is that of the non-magnetic component of the MISMA model atmosphere.

The actual model atmospheres are described using 23 parameters: the temperature of the non-magnetic component at four heights, a global scaling factor for the temperature of the magnetic components (item 1 above), two magnetic field strengths at the bottom of the atmosphere (or BID, which stands for Bottom of Integration Domain) (item 3), two occupation fractions at BID (i.e., the fraction of atmospheric volume occupied by each magnetic component; item 2), two velocities at BID (item 5), two magnetic field inclinations (item 4), one magnetic field azimuth (item 4), four parameters to define the distribution of microturbulent velocities (two for the magnetic components, and two for the non-magnetic component), three parameters to account for the stray light (item 6), one macro-turbulent velocity (which simulates instrumental broadening plus macro-turbulence of solar origin) and, finally, the maximum pressure at BID. The latter varies to assure that the model atmosphere embraces the region between  $\log \tau_c = 1$  and  $\log \tau_c = -4$  (with  $\tau_c$  the continuum optical depth at 6302 Å). This range of optical depths guarantees

that the lines Fe I  $\lambda 6302.5$  Å and Fe I  $\lambda 6301.5$  Å are entirely formed within the bounds of the model atmosphere. Recovery of the complete atmospheric structure from these 23 parameters is described in Sánchez Almeida (1997)<sup>3</sup>. These 23 parameters must be set during the least-squares fitting procedure. Although the number of free parameters seems large, it has to be compared with the 536 different observed quantities to be fitted (67 wavelengths per line and per Stokes parameter; see Fig. 3). These observables are not fully independent (e.g., the finite spectral resolution links neighbor wavelengths, and the radiative transfer couples the four Stokes parameters), but the author believes that the number of observables is so large compared with the number of free parameters that the number of *independent* observables almost certainly exceeds 23.

Figure 2 illustrates the kind of complex distribution of magnetic field lines that our schematic model MISMA may be modeling. Field lines like these are represented by our IC as, e.g., the model MISMA in Fig. 4. If the micro-structure of the atmosphere is optically-thin then the emerging spectrum does not depend on details of the atmosphere but only on its average properties (Sánchez Almeida et al. 1996). Therefore, describing a messy bunch of field lines with only two components is consistent with our MISMA assumption. Obviously, we cannot infer details of the micro-structure but volume average properties. In particular, we are insensitive to the size of the micro-structures, which we consider to be optically-thin and so smaller than 100 km. The cartoon in Fig. 2 represents magnetic field lines existing in a single resolution element. The field lines are aligned approximately radially from the sunspot center, having different azimuths and inclinations. Figure 2a shows a view from the top of the 3-dimensional distribution of field lines. They show a global radial orientation but, due to slight misalignments and swings, many different field lines overlap along any line-of-sight. The axes, given in Mm, are for guidance only. Figure 2b represents a side view of the same distribution of field lines. Different magnetic field inclinations coexist in the resolution elements.

The MISMA scenario and the requirements used for sunspot inversions are basically those that successfully reproduce the Stokes profiles observed in plage, network and internetwork regions (Sánchez Almeida 1997; Sánchez Almeida & Lites 2000; Socas-Navarro & Sánchez Almeida 2002). The main difference being the inclination of the magnetic fields, and the different temperatures of the magnetic components and the background. The similarities between scenarios probably reflects both the degeneracy of the radiative transfer for MISMA and the fact that the employed MISMA scenario grasps the essential degrees of freedom required to reproduce most asymmetries found in the photosphere.

As explained above, there are two magnetic component in each model MISMA. They will be denoted as minor and major depending on which one has largest  $\alpha\rho$ , i.e., the largest product of occupation fraction  $\alpha$  times density  $\rho$ . Consequently, the major component is the one containing most of the mass of the atmosphere. This intuitive classification is also used in Paper II. Here, however, the component of largest  $\alpha\rho$  may change along the atmosphere, making the definition ambiguous. Fortunately, the change occurs in a small fraction of inversions (3%) and, even in these cases, it only affects a few superficial layers. (The classification is based on  $\alpha\rho$  at the bottom of the atmosphere.)

<sup>2</sup> However, this hypothesis makes our model insensitive to the temperature variations associated with the smallest penumbral filaments observed by, e.g., Scharmer et al. (2002).

<sup>3</sup> But note the misprint in equation (13).

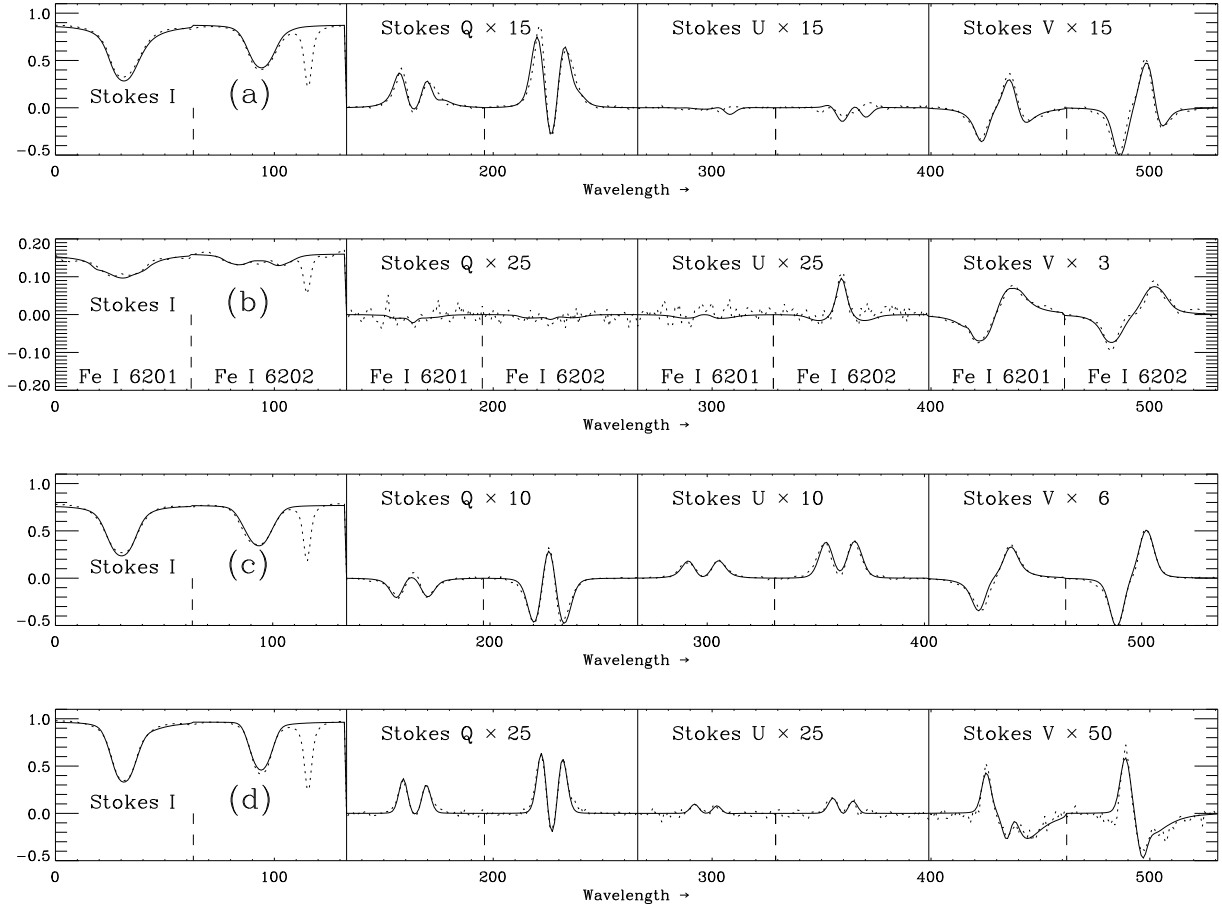


FIG. 3.— Examples of the quality of the fits provided by the MISMA inversions. They show Stokes  $I$ ,  $Q$ ,  $U$  and  $V$  profiles of Fe I  $\lambda 6301.5$  Å and Fe I  $\lambda 6302.5$  Å. (The different types of profiles are separated by vertical solid lines, and the division between Fe I  $\lambda 6301.5$  Å and Fe I  $\lambda 6302.5$  Å is indicated by vertical dashed lines.) The solid lines are synthetic profiles whereas the dotted lines show observations. (a) Profiles in the limb-side penumbra. (b) Profiles in the umbra. (c) Profiles in the center-side penumbra. (d) Profiles outside the limb-side penumbra. The abscissae represent the pixel number in an array used to carry out the fits. Within each type of Stokes profile, wavelengths increase to the right, with a gap between Fe I  $\lambda 6301.5$  Å and Fe I  $\lambda 6302.5$  Å to exclude a telluric line. Note the large asymmetries of some of the profiles, and the fair fit provided by the inversions; e.g., Stokes  $V$  in (a) and (d).

### 3.2. Strategy for inversion

First, the center of the sunspot was set by trial and error. We minimize the departures from axi-symmetry of the distribution of observed continuum intensities. The chosen center is 1.3 Mm away from the darkest point in the umbra. The resulting intensity distribution is fairly symmetric, leading to a sunspot radius of about 17 Mm, which is the value adopted in the paper.

We choose for inversion all those pixels within 24 Mm from the sunspot center having a degree of polarization larger than 0.5% (average polarization over a bandpass 75 mÅ wide in the blue wing of Fe I  $\lambda 6302.5$  Å). This criterion yields 10130 different pixels encompassing the entire sunspot (Fig. 1). We have carried out an inversion for each one of these pixels using the IC described in Paper I and the scenario presented in § 3.1. The strategy for inversion is slightly different from the one in Paper II. We also begin by classifying all Stokes profiles using a principal component analysis scheme. This procedure sorts the observed Stokes profiles according to similarities in shape. We start the inversion at the sunspot center, and then proceed with the closest profile according the classification. However, rather than using the last retrieved atmosphere to

initialize each new inversion, we look up in a data base with all previously inverted synthetic profiles. The atmosphere of the closest one (in a least squares sense) is chosen for initialization. The process is repeated to completion of the 10130 sets of Stokes profiles. Each automatic inversion was visually inspected before acceptance. Failures were re-started from a different model atmosphere until the agreement was satisfactory.

### 3.3. Quality of the fits

Figure 3 shows four examples of the quality of the fits provided by the MISMA inversions. We have chosen the Stokes profiles at four positions on the sunspot, (a) limb-side penumbra, (b) umbra, (c) center-side penumbra, and (d) outside the penumbral border defined by the continuum image (the letters correspond to the labels on the figure, whereas limb-side and center-side refer to the portion of penumbra closest to or farthest from the solar limb). These four regions produce Stokes profiles with the variety of shapes to be reproduced with the inversions, including severe Stokes asymmetries. The Stokes  $V$  profile in Fig. 3a shows the so-called cross-over effect (Grigorjev & Katz 1972; Golovko 1974), with Stokes  $V$  having three or more lobes. It occurs

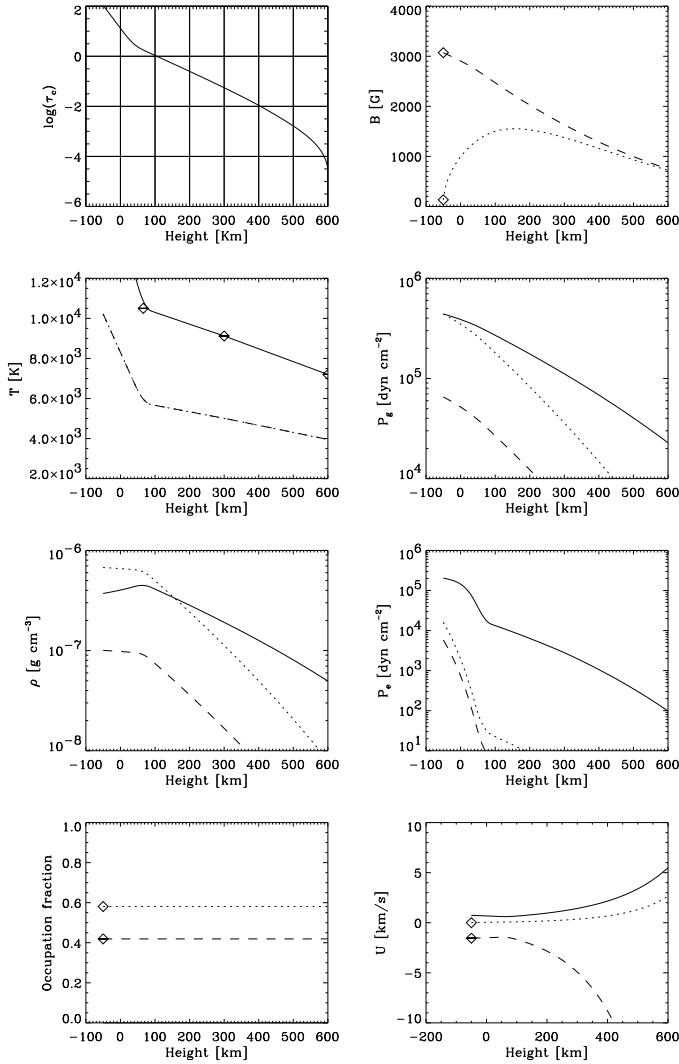


FIG. 4.— Typical model MISMA retrieved by the IC used in this work. It reproduces the profiles in Fig. 3a. The different panels represent the variation with height in the atmosphere of various physical parameters (from left to right and from top to bottom): the continuum optical depth, the magnetic field strength, the temperature, the gas pressure, the density, the electron pressure, the occupation fraction, and the speed along field lines. Except for the upper-left panel, the type of line identifies the three components of the model MISMA; the solid lines correspond to the non-magnetic component and the dotted and dashed lines to the magnetic components. The diamonds indicate the free parameters of the model, from which the entire stratification of the atmosphere has been deduced. Note that the atmosphere is only meaningful within the range of optical depths where the observed lines are formed (e.g., the drop of major component magnetic field strength below  $\log \tau_c = 0$  is not significant;  $\log \tau_c = 0$  occurs at 100 km).

in the neutral line, where the mean magnetic field is perpendicular to the line-of-sight, and Stokes  $V$  should be zero if the magnetic field were spatially resolved (Makita 1986; Sánchez Almeida & Lites 1992). Despite the quality of the fits, we would like to point out that they are not as good as for the quiet Sun network and internetwork profiles described in Paper II and Socas-Navarro & Sánchez Almeida (2002). We have not been able to pin down the cause, however, it obviously implies that the scenario adopted for inversion suits better the conditions in the quiet Sun.

Yet another hint of the quality of the fits is provided by the ability to reproduce the observed net circular polarization, a

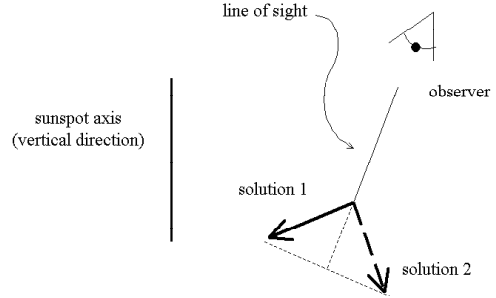


FIG. 5.— Schematic showing the two possible solutions compatible with a given Zeeman absorption. The two have the same magnetic field component along the line-of-sight, and differ by  $180^\circ$  in azimuth. We have tried to select the solution that converges toward the sunspot axis (solution 1). (We deal with a negative polarity sunspot, so that solution 1 tends to be anti-parallel to the vertical direction.)

result analyzed in detail in § 4.6.

### 3.4. Removal of the azimuthal ambiguity

A rotation of the magnetic field vector by  $180^\circ$  about the line-of-sight does not modify the Zeeman absorption (e.g., Unno 1956; Landi Degl’Innocenti 1992). This leads to the well known azimuthal ambiguity of the magnetic field derived from Zeeman magnetometry, which has to be sorted out before proceeding. Since the MISMA model atmospheres have two magnetic components (§ 3.1), each one with this  $180^\circ$  ambiguity, each pixel has four different magnetic configurations compatible with the observation<sup>4</sup>. Among them, we chose the one that best fits in a global magnetic field that converges toward the sunspot core, and is as smooth as possible. First, we begin with the major components of all pixels (i.e., with the components containing most of the mass; see §3.1). The smoothest solution is obtained after an iterative procedure where the direction of the magnetic field vector in a given pixel is compared with the direction of the mean field provided by the surrounding pixels. Then the solution closest to the mean direction is chosen. This procedure is applied to each pixel and then iterated to a point where no pixel over the full FOV has to be modified. The iterative procedure starts by choosing that solution representing a magnetic field converging toward the sunspot core (see Fig. 5). If the two solutions of a pixel are of this kind, then the closest to the sunspot radial direction is chosen. We tried various box sizes to compute the local average (from  $3 \times 3$  pixels to  $15 \times 15$  pixels). The disambiguation of the sunspot magnetic field is almost insensitive to this parameter, which mostly affects the field outside the visible sunspot. We finally adopted  $10 \times 10$  pixels, which provides a fair compromise. Once the map of the major component is retrieved, we choose that minor component solution whose direction is closest to the major component direction. The algorithm sketched above provides a fairly axi-symmetric mag-

<sup>4</sup> Two remarks are in order. First, neither the azimuth nor the inclination of each component vary with height in the atmosphere (§ 3.1). Having varying azimuths and inclinations would make the ambiguity intractable. Second, the Doppler shifts only depend on the projection of the velocity along the line-of-sight. Since we assume magnetic-field-aligned motions, all these four solutions have the same velocity along the line-of-sight and therefore are compatible with the inferred velocity field.

netic field distribution centered at the sunspot core inferred from the continuum intensity. Figure 6 shows maps of inclination and azimuth for the major components. Figure 7 shows the same maps for the minor components.

### 3.5. Setting a common scale of heights for the full inversion

Each pixel has been inverted independently from the rest. Therefore each one has its own scale of heights. Part of the analysis of the forthcoming sections becomes more meaningful when carried out in a common scale of heights for the whole sunspot. We have set such common scale assuming that the total pressure (gas pressure plus magnetic pressure) is similar among neighbor pixels. (This approach was successfully applied in Paper II; § 4.2.) The absolute vertical scale of each pixel is set by comparison with the pressure of the nearest neighbors whose absolute scale is already known. We minimize the differences between the logarithms of the total pressures allowing only for a global shift of the scale of heights. The procedure starts at the center of the sunspot and then continues to the penumbral border, and beyond. The zero of the absolute scale is set by the layer  $\tau_c = 1$  in the stray light component of the model atmospheres far from the sunspot (further than 23 Mm; see Fig. 1). These model atmospheres represent the non-magnetic Sun so that the absolute heights are referred to the base of the non-magnetic photosphere. The uncertainty introduced by the assumption that the total pressure does not change between adjacent pixels is discussed in Appendix A. It is smaller than 100 km for determining the Wilson depression of the umbra, and it becomes negligible small when computing pixel-to-pixel variations ( $\leq 4$  km).

## 4. MAIN RESULTS OF THE MISMA INVERSION OF A SUNSPOT

### 4.1. Occupation fraction

As described in § 3.1, the model MISMA used for inversion have three different components, two magnetic plus a non-magnetic background<sup>5</sup>. The *occupation fraction* (OCF) is the fraction of atmospheric volume occupied by each one of them. In principle the OCFs vary with height in the atmosphere (Paper I). However, height variations are expected only when the OCF of the background differs from zero, since the magnetic OCFs grow at the expense of non-magnetic volume. Since the OCF of the background is very small (see below), the OCF of the magnetic components remains basically constant with height. Figure 8 shows the retrieved OCFs as a function of the radial distance from the sunspot center. We plot the values at the height in the atmosphere where  $\log \tau_c = -1$ , an optical depth where most of the atmospheric information extracted from the inversion comes from. The shaded areas represent plus and minus one standard deviation among all the points at the same radial distance. Note that the major component has the largest OCF all the way from the umbra to the sunspot surroundings. This result is not a trivial consequence of the definition of major and minor, since the definition also involves mass densities (§ 3.1). The major component OCF goes from more than 90% in the umbra to about 70% in the outer penumbra (the solid line in Fig. 8).

<sup>5</sup> The non-magnetic background should not be confused with the stray light component included in the fits (§ 3.1, item #6). The stray light component will not be discussed in the paper since it shows a rather expected behavior similar to the non-magnetic stray light component deduced from the Milne-Eddington inversions of the same sunspot. The stray light fill factor goes from 2% in the umbral core to 25% at the penumbral border.

The minor component is significantly different from zero only outside the umbra (from 5 Mm on; Fig. 8, the dashed line). It occupies 30% of the penumbral volume.

### 4.2. Magnetic field inclinations and azimuths

Figure 6 shows inclinations and azimuths of the major component. Figure 7 shows maps of the same parameters for the minor component. The actual values are better appreciated in Fig. 9, where we represent the mean azimuths and inclinations, as well as the standard deviation of these quantities among those points at the same distance from the sunspot center. (For a visual definition of vertical inclination and relative azimuth, see Fig. 10.) Both the major component and (to less extent) the minor component follow the radial direction. The relative azimuth with respect to the radial direction is of the order of  $180^\circ$ , as it should be for a radial magnetic field in a negative polarity sunspot (Fig. 9b). (The properties of the minor component for distances smaller than 5 Mm are excluded. The minor component of these points does not contribute to the observed signals and therefore, any inference based on it results unreliable.) The magnetic field inclination of the major component follows a variation with radial position typical of sunspots (from say,  $170^\circ$  at the sunspot core, to about  $15^\circ$  off the horizontal at the sunspot boundary; see., e.g., Fig. 9 in Lites et al. 1993). Together with this smooth and expected behavior, the minor component is (with large scatter but beyond any doubt) always less inclined than the horizontal (see the dashed line in Fig. 9a). We deal with a negative polarity sunspot and, therefore, visualizing the magnetic topology from the inclination is not so straightforward. The cartoon in Fig. 11 has been laid out to illustrate the magnetic topology. This inclination of the minor component is common to the whole penumbra, implying that magnetic field lines are returning to the solar interior over the entire penumbra. This is possibly the biggest surprise of these MISMA inversions. As we will discuss in connection with the mass flows (§ 4.5), inferences of magnetic fields returning to the sub-photosphere at the outer penumbra and beyond do exist in the literature (Rimmele 1995; Westendorp Plaza et al. 1997). The presence of magnetic field lines that return throughout the penumbra is new, though.

### 4.3. Magnetic field strengths and fluxes

Figure 12 shows the variation of the magnetic field strength with the distance from the sunspot center. The field strength varies with height, so we plot the value at  $\log \tau_c = -1$ . The two magnetic components are shown separately. (The field strength of the minor component in the umbra is not included since its occupation fraction is negligible and therefore its value dubious; § 4.1.) The field strengths go from 3 kG at the sunspot core to 1 kG at the transition between penumbra and its surroundings. The observed variation is typical of sunspots (e.g., Fig. 9 in Lites et al. 1993). More interesting is the systematic difference of field strength between components. The mean field strength of the minor component is about 200 G larger than that of the major component. This excess is significant. The dispersion among the field strengths of all the pixels at a radial distance is also of the order of 200 G (the shaded regions in Fig. 12). The dispersion of the mean is reduced by a factor square root of the number of pixels contributing to each radial point. Typically, several hundred pixels contribute to the mean so that the uncertainty of the mean is only a few tens of G, and so, well below the observed 200 G difference.

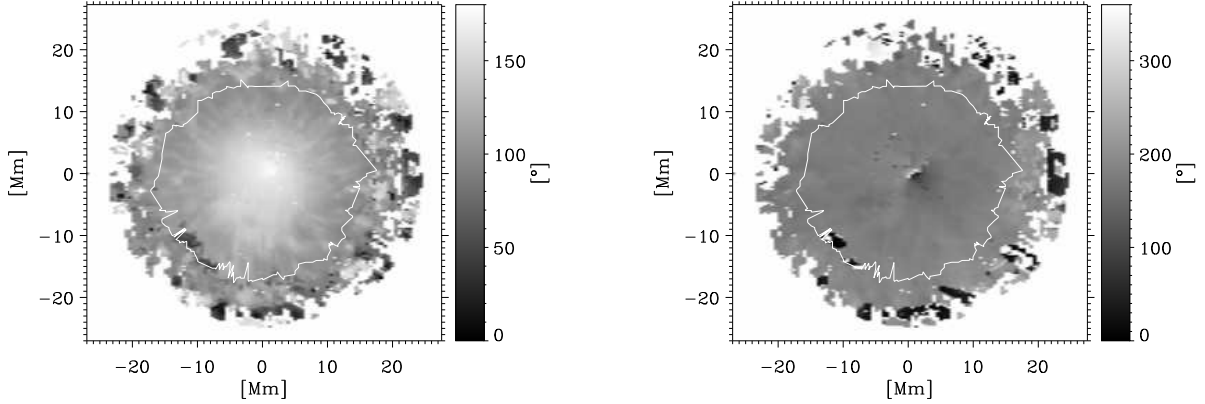


FIG. 6.— Maps of the inclination (left) and the local azimuth (right) of the major magnetic component of the MISMA inversions. The inclinations are scaled between  $0^\circ$  and  $180^\circ$  whereas the azimuths go from  $0^\circ$  to  $360^\circ$ . Note the axi-symmetry of the retrieved magnetic fields. The white outline corresponds to the external penumbral border (see Fig. 1).

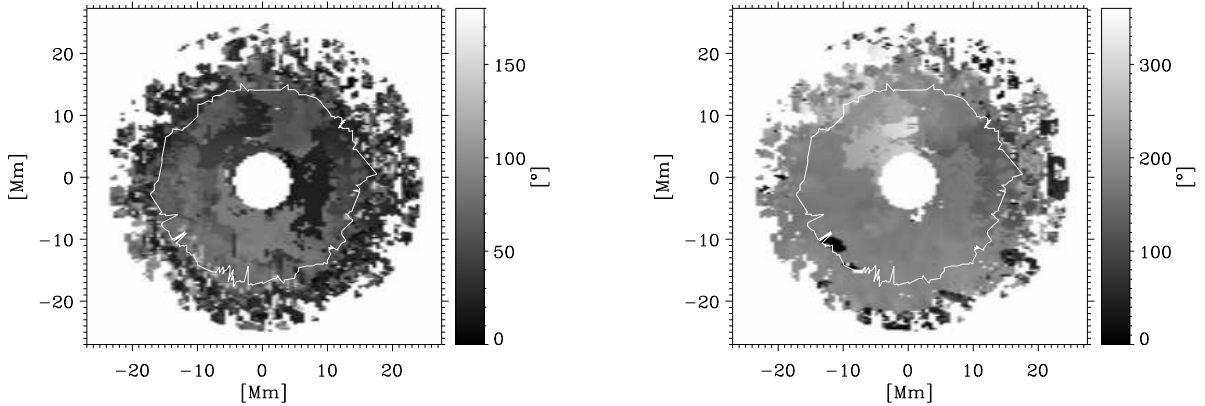


FIG. 7.— Maps of the inclination (left) and the local azimuth (right) of the minor magnetic component of the MISMA inversions. They are represented as in Fig. 6. The umbra is empty since the minor component is absent in this region.

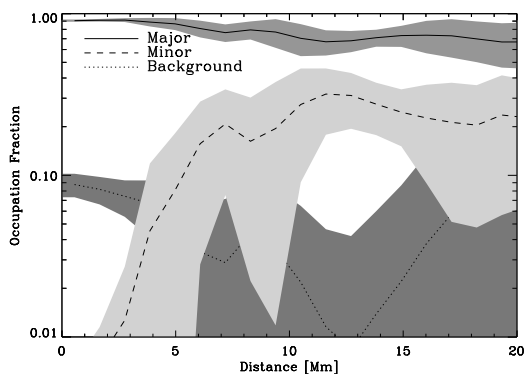


FIG. 8.— Radial variation of the fraction of resolution element occupied by each component of the model MISMA. The radial distance is given in Mm, and all occupation fractions are evaluated at  $\log \tau_c = -1$ . The shaded regions represent the standard deviation among the points at a distance from the sunspot core.

The error bars of the mean are also included in Fig. 12, but they go almost unnoticed due to their small values.

The excess of field strength creates a surplus of magnetic pressure and, consequently, a deficit of gas pressure in the mi-

nor component. Let us assume that the minor and major components of the same or neighbor resolution elements are connected by field lines. (We have not been able to come up with any other possibility to understand the presence of field lines pointing up and down throughout the penumbra. However, this connection between the field lines of the minor and major components does not result from the inversions and is speculative.) Then the gradient of gas pressure between minor and major components is bound to drive a mass flow. This is nothing but the siphon flow mechanism invoked to explain the Evershed flow (Meyer & Schmidt 1968; Thomas & Montesinos 1993). The seemingly small difference of field strength that we infer can drive a very fast flow, as attested by a simple order of magnitude estimate. For a typical magnetic field strength in the penumbra  $B$  of 2 kG,

$$\Delta B/B \sim 0.1. \quad (1)$$

The square velocity difference produced by a gas pressure excess  $\Delta P_g$  is

$$\Delta U^2 \sim -\frac{2\Delta P_g}{\rho}, \quad (2)$$

where we have used the equation of motion for a horizontal thin flux tube (e.g., Spruit 1981). Since the gas pressure dif-

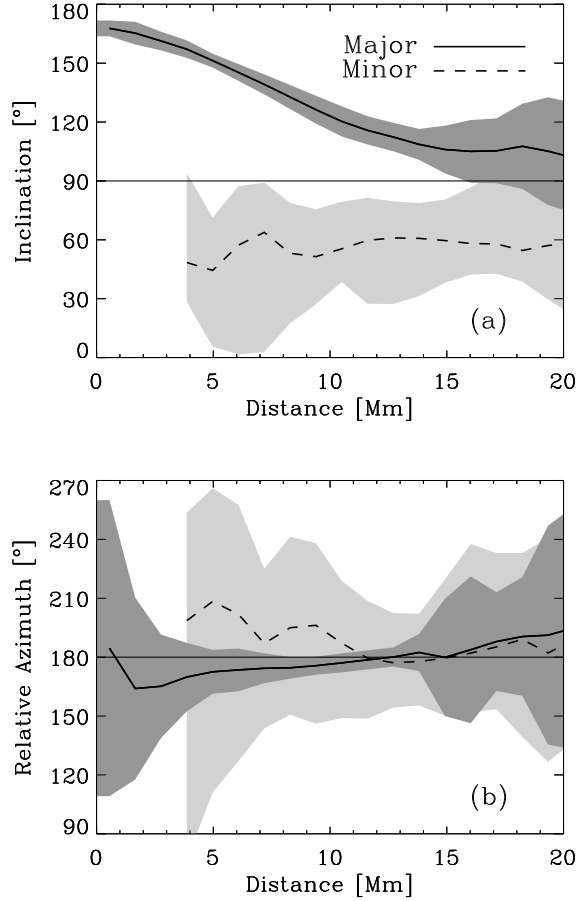


FIG. 9.— Radial variation of the magnetic field inclination (a) and relative azimuth (b) of the two magnetic components of the model MISMA. The lines represent the mean values among those pixels at a distance from the sunspot center. The shaded regions correspond to the standard deviation. Each type of line identifies one component, as described by the inset in (a).

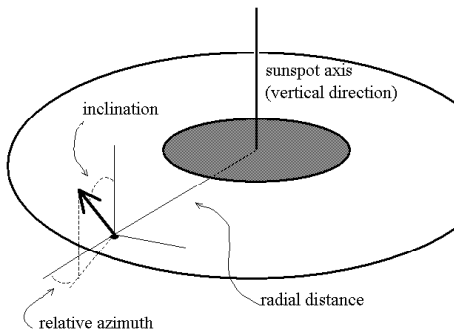


FIG. 10.— Schematic to show the *inclination* and *relative azimuth* used to present the results of the inversion. It displays the coordinate system used to describe the magnetic field vector (the thick arrow) at a given radial distance from the sunspot core. The relative azimuth is the azimuth in a local cylindrical coordinate system where the radial direction is the radial direction from the sunspot center. The inclination is inclination with respect to the vertical direction. The coordinate system is different for different pixels. For the sake of clarity, we show a magnetic field of *positive* polarity, however, the true sunspot is of *negative* polarity. For this reason the relative azimuths tend to be 180° (Fig. 9b).

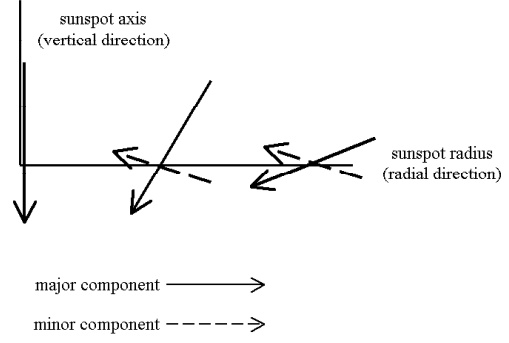


FIG. 11.— Schematic showing the direction of the major and minor components relative to the vertical and radial directions. It shows the components at three different radial distances. Since we deal with a negative polarity sunspot, the magnetic field points downward at the sunspot axis.

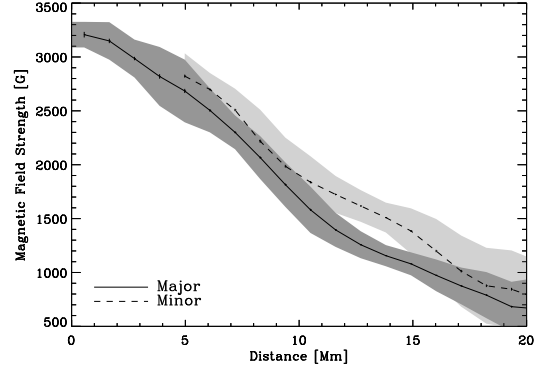


FIG. 12.— Radial variation of the magnetic field strength of the two magnetic components. The mean field strength of the minor component is 10% larger than the strength of the major component. The shaded regions represent the standard deviation among all the points at a distance from the sunspot core. The lines correspond to the mean values. Error bars for these mean values are also included, but they go unnoticed due to their small values.

ference is due to the magnetic field strength difference, then

$$\Delta P_g = -\frac{B^2}{4\pi} \frac{\Delta B}{B}. \quad (3)$$

Using equations (2) and (3), one finds,

$$(\Delta U^2)^{1/2} \sim \left[ \frac{B^2}{2\pi\rho} \frac{\Delta B}{B} \right]^{1/2}, \quad (4)$$

with the symbol  $\rho$  standing for the density. For typical densities at  $\log \tau_c \sim -1$  ( $\sim 10^{-7}$  g cm $^{-3}$ ; see § 4.4),

$$(\Delta U^2)^{1/2} \sim 8 \text{ km s}^{-1}. \quad (5)$$

This velocity is similar to the minor component velocities inferred from the inversions; see § 4.5.

According to the current paradigm, a large fraction of the sunspot magnetic flux emerges in the penumbra (e.g. Solanki & Schmidt 1993). It leads to the concept of deep penumbra, where the boundary between magnetized plasmas and non-magnetic environment occurs well below the observed photospheric layers. To our surprise, the model sunspot turns out to have very little vertical magnetic flux across the penumbra. Our finding does not imply a shallow penumbra, though. It follows from the large amount of return

flux in the penumbra. The two magnetic components tend to have vertical magnetic field strengths with opposite signs (§ 4.2 and Figs. 9 and 11). This leads to a cancellation of the average vertical component of the field strength  $\langle B_z \rangle$ . (The angle brackets  $\langle \rangle$  are used in the paper to represent volume average, i.e., an average weighted with the OCFs.) The mean vertical component at  $\log \tau_c = -1$  is shown in Fig. 13a. It tends to zero in the external penumbra (say, for distances between 10 Mm and 16 Mm). However, the unsigned mean  $\langle |B_z| \rangle$  is certainly different from zero. Such difference between signed mean and unsigned mean produces significant differences between the signed and unsigned magnetic fluxes of the sunspot. The signed vertical magnetic flux of those points with radii between  $r_1$  and  $r_2$  is

$$\Phi_z(r_1 < r < r_2) = 2\pi \int_{r_1}^{r_2} r \langle \widehat{B_z} \rangle dr, \quad (6)$$

with  $\langle \widehat{B_z} \rangle$  the azimuthal average of  $\langle B_z \rangle$ ,

$$\langle \widehat{B_z} \rangle = \frac{1}{2\pi} \int_0^{2\pi} \langle B_z \rangle d\chi, \quad (7)$$

and  $\chi$  the absolute azimuth of each point. (The unsigned mean is formally identical to equation [6] replacing  $\langle B_z \rangle$  with  $\langle |B_z| \rangle$ .) Figure 13b shows the integrand of equation (6), i.e., the contribution of each radius to the sunspot flux. It is clear how the penumbra makes a significant contribution to the unsigned flux of the sunspot, but little to the signed flux. Table 1 quantifies how much. It lists the vertical magnetic flux of the sunspot, the umbra and the penumbra. The signed flux of the sunspot is 33% smaller than the unsigned flux. Flux cancellation primarily occurs in the penumbra (58% reduction) and very little in the umbra (9% reduction). The cancellation at the penumbral border is more than 80%, a result which could be naturally explained if field lines emerge, bend over, and return in a distance similar to the angular resolution. (A detailed discussion about the physical interpretation of such speculative arguments is deferred to another paper; Sánchez Almeida 2005.) The penumbra has as much unsigned flux as the umbra, but only 40% of the signed flux. Table 1 also includes the fluxes of a standard model sunspot without return flux. The flux of the standard model sunspot lies in between our signed and unsigned fluxes.

#### 4.4. Mass Density

Figure 14 shows the variation of the density along the radial direction at  $\log \tau_c = -1$ . The densities of the major component are not very different from the densities of the quiet Sun at this optical depth. Note, however, how the density of the minor component is five times smaller. The association of minor and major, which involves the density. In addition, the enhanced magnetic field strength of the minor component described above demands a decrease of gas pressure and, consequently, a decrease of density. (Recall that major and minor temperatures are forced to be identical; § 3.1.)

#### 4.5. Motions and the Evershed effect

All motions are aligned along the magnetic field lines. This is a constraint directly imposed on the model MISMA (§ 3.1).

The velocity pattern retrieved from the inversion is simple and regular; see Fig. 15. The minor component, with the

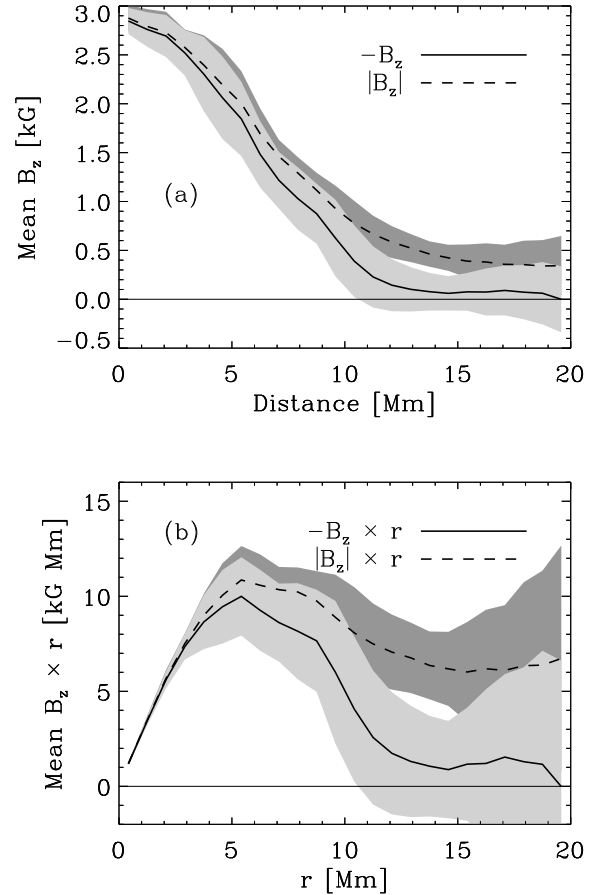


FIG. 13.— (a) Volume average of the vertical magnetic field strength. The solid line shows the signed mean whereas the dashed line corresponds to the unsigned mean. Note the large difference in the external penumbra (say, for distances between 10 and 16 Mm.) The shaded regions represent plus-minus one standard deviation among all those points at the same distance from the sunspot center. (b) Average vertical field times distance to the sunspot center ( $r \equiv$  Distance). The integral of this quantity between two radii provides the vertical magnetic flux.

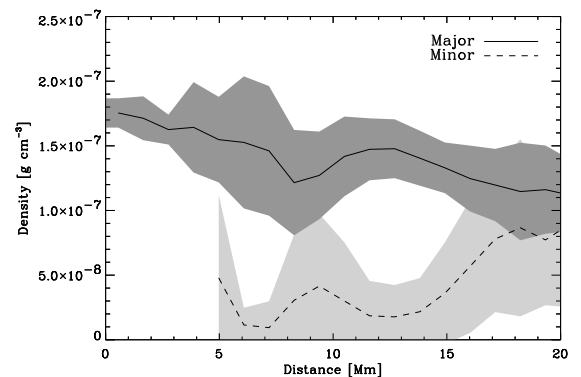


FIG. 14.— Radial variation of the density of the two magnetic components. The major component is five times denser than the minor component. Distances are given in Mm from the sunspot center.

lowest mass density and the highest magnetic field strength, has very large velocities. They typically reach  $10 \text{ km s}^{-1}$  at  $\log \tau_c = -1$ . The major component shows much smaller val-

TABLE 1  
VERTICAL MAGNETIC FLUX ACROSS THE SUNSPOT

		Unsigned	Signed	Reference <sup>a</sup>
$\Phi_z(0 < r < R_S)$	full sunspot	$\Phi_0 = 7.3 \times 10^{21}$ Mx	$0.67 \Phi_0$	$0.99 \Phi_0$
$\Phi_z(R_S/2 < r < R_S)$	penumbra <sup>b</sup>	$\Phi_1 = 0.49 \Phi_0$	$0.42 \Phi_1$	$0.83 \Phi_1$
$\Phi_z(R_S/\sqrt{2} < r < R_S)$	outside penumbra <sup>c</sup>	$\Phi_2 = 0.25 \Phi_0$	$0.20 \Phi_2$	$0.63 \Phi_2$
$\Phi_z(0 < r < R_S/2)$	umbra	$\Phi_3 = 0.51 \Phi_0$	$0.91 \Phi_3$	$1.14 \Phi_3$

<sup>a</sup>Normalized sunspot model in Solanki (2000), Table 14.34, with a maximum vertical field strength of 2.8 kG and the radius of our sunspot.

<sup>b</sup>We assume the umbral radius to be half of the sunspot radius  $R_S$ .

<sup>c</sup>Penumbral rim having half of the sunspot area.

ues. Both velocities are directed radially outward along the field lines. Since the magnetic field lines are not horizontal (see, Fig. 9 and § 4.2) the velocities have both horizontal and vertical components. Figure 16 shows the radial velocity  $U_r$  and vertical velocity  $U_z$  of the major (top) and minor (bottom) magnetic components at  $\log \tau_c = -1$ . The vertical velocity of the major component is positive, meaning that it is directed upward. The vertical velocity of the minor component is directed downward. This downward directed velocity occurs all over the penumbra (Fig. 15). The small upward motions in the umbra (Fig. 16, top) are consistent with the lack of motion found by Beckers (1977) considering the uncertainties of the absolute scale of velocities (§ 2).

The finding of upward motions in the inner penumbra and downward motions in the outer penumbra is now common in the recent literature (Rimmele 1995; Schlichenmaier & Schmidt 2000; del Toro Iniesta et al. 2001; Bellot Rubio et al. 2003; Tritschler et al. 2004). To the best of our knowledge, we are the first to infer ubiquitous downward motions in a penumbra. (Recall, ubiquitous upward and downward motions.) This seemingly inconsistency of our finding with previous works is probably an artifact produced by the spatially unresolved structure of the flows. Most techniques employed so far assume uniform velocities in the resolution element. However, observations show with insistence the presence of several velocity components (Bumba 1960; Stellmacher & Wiehr 1971; Wiehr 1995; Rüedi et al. 1999). In our case we infer two very different types of motion<sup>6</sup>. When the observations are interpreted as a single resolved component, the *measured* velocity corresponds to some kind of ill-defined mean value of the actual velocities<sup>7</sup>. Since (a) the true velocities can be extremely high (e.g., Fig. 16), (b) there are both upward and downward motions, and (c) the residual velocities are very small, *measuring* upflows or downflows depends on subtleties of how the various motions contribute to the mean values. The contribution depends on the physical properties of the penumbral atmospheres, as well as on method employed to measure (the spectral line, the portion of line profile that is employed, the method used to assign Doppler shifts, and so on). In order to show that this interpretation of the systematic flows deduced by others is consistent with our inversions, we have also

<sup>6</sup> The finding of two types is an idealization that we impose, and it should be understood as the need for more than one mean component to describe the observed line shapes.

<sup>7</sup> Like the well-known convective blueshift of the photospheric lines (e.g., Dravins 1982). If this convective blueshift is interpreted as a net motion, one infers a significant global expansion solar surface, able to double the solar radius in less than a month.

measured the Evershed flow of our sunspot with one of the techniques used in single component inferences. Downflows at the penumbral rim have been observed using the displacement of the Stokes  $I$  bisector at the line wings (e.g., Rimmele 1995; Tritschler et al. 2004). We compute the bisector corresponding to each observed Stokes  $I$  profile of Fe I  $\lambda 6301.5$  Å, the line with lowest Zeeman sensitivity in the spectra. The azimuthally averaged shifts of the bisectors are represented in Fig. 17b (the solid line with asterisks). (The azimuthal average of the line-of-sight velocity cancels the contribution of the horizontal motions, so that only vertical velocities remain; see, e.g., Schlichenmaier & Schmidt 2000.) The simulated bisector-based measurement shows upflows in the inner penumbra and downflows in the outer penumbra, in agreement with single component estimates (several representative measurements from the literature are included in Fig. 17). The bisector-based mean velocity is qualitatively different from the true mean velocity of our inversions (the solid lines with error bars in Fig. 17). This OCF weighted mean velocity shows downflows everywhere, meaning that the minor component dominates the average. However, the nature of the curve changes when the mean is computed weighting each component with its mass (i.e., mass density times OCF). Then the vertical velocity is not far from to some of the mean velocities of the literature (compare the plain solid line in Fig. 17b with, e.g., the dotted line). One may think that the scatter among individual velocities in Fig. 16 questions the small mean velocities shown in Fig. 17. However, small differences of mean velocities are significant since hundreds of independent inversions contribute to each mean value. The scatter of the mean decreases as the square root of the number of pixels contributing to the mean, a factor of the order of 30 at the penumbral edge. The plain mean velocities in Fig. 17 include these formal error bars, supporting the reliability of our mean velocities. (The errors for the mass weighted mean are similar.) Formal error bars for the mean velocities are also included in Fig. 16.

#### 4.6. Net Circular Polarization

The presence and behavior of Net Circular Polarization (NCP) created by individual spectral lines has stimulated some of the important advances on the penumbral magnetic field structure. Any consistent penumbral model should be able to reproduce its properties. Our semi-empirical sunspot does it. The NCP is defined as

$$\text{NCP} = \int_{\lambda_1}^{\lambda_2} V(\lambda) d\lambda, \quad (8)$$

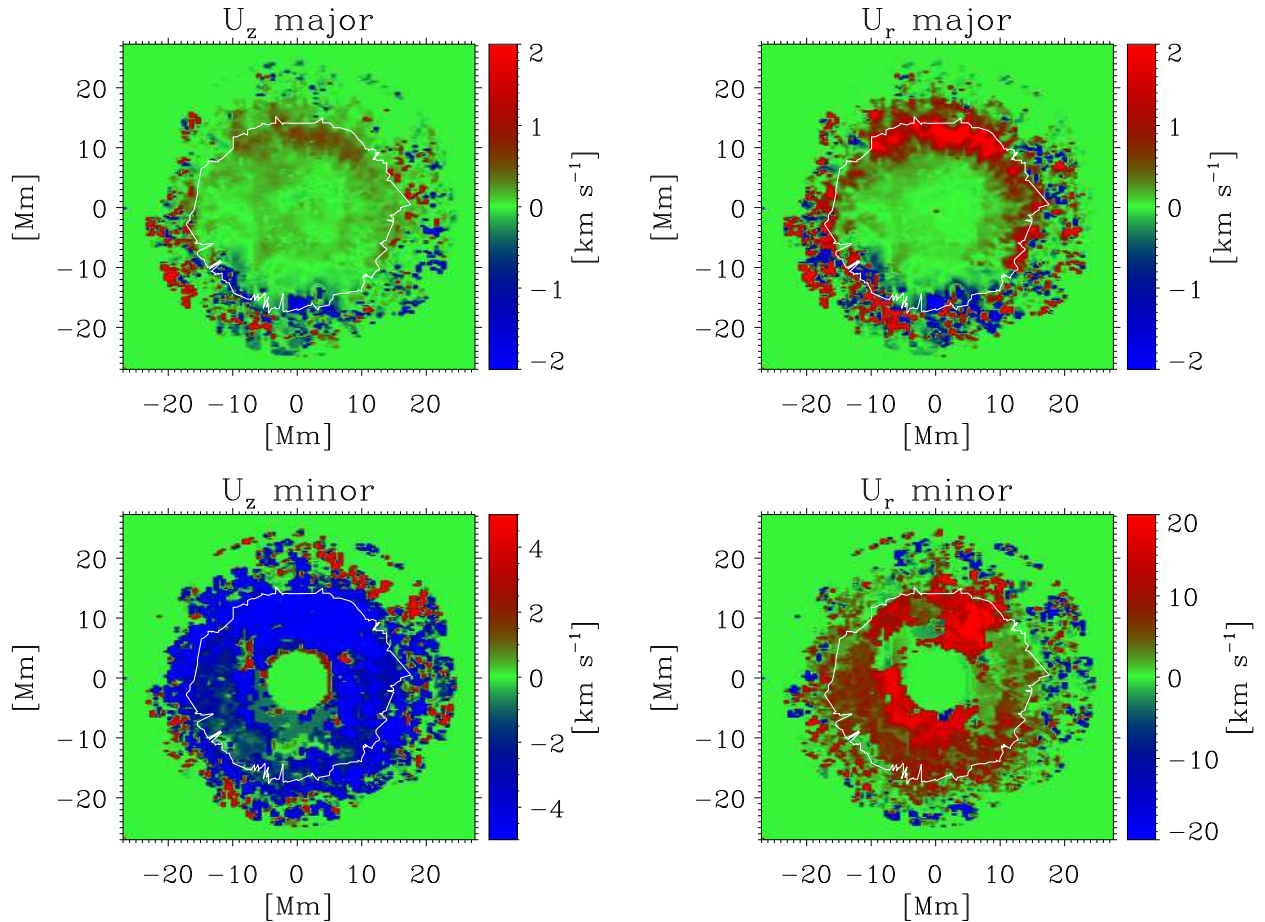


FIG. 15.— Horizontal  $U_r$  and vertical  $U_z$  velocities of the two magnetic components at  $\log \tau_c = -1$ . The equivalence between the color code and the velocity differs for the different plots, as it is indicated by the vertical bars. Positive vertical velocities correspond to upward motions. Positive radial velocities correspond to outward motions. First, note the large velocities of the minor component (the two figures at the bottom), as compared to the velocities of the major component (the two figures at the top). Second, note the downward motions of the minor component plasma occurring over the entire penumbra. The minor component signals have been set to zero in the umbra, since the minor component does not contribute to the umbral spectrum. The white contour outlines the border of the continuum sunspot, i.e., the transition between the penumbra and the surrounding photosphere (c.f. Fig. 1).

with the integral extending a full line profile included between wavelengths  $\lambda_1$  and  $\lambda_2$ . Figure 18 shows a scatter plot of synthetic versus observed NCP of Fe I  $\lambda 6302.5 \text{ \AA}$ . Although the observed values tend to be larger than the synthetic ones, the syntheses grasp the observed behavior. The maximum value is around  $-3 \text{ m\AA}$  and the signs are preserved. In addition, both the observed NCP and the synthetic NCP follow the general rules found by Illing et al. (1974a,b) and Makita (1986), and summarized in Sánchez Almeida & Lites (1992, § 4); the extreme NCP is negative (as the sunspot polarity) and occurs at the limb-side penumbra where the Stokes  $V$  profiles show the cross-over effect (profiles with three or more lobes like those in Fig. 3a).

In order to add one more piece of evidence supporting the consistency of the model sunspot, we synthesized the NCP produced by Fe I  $\lambda 15648 \text{ \AA}$ . The NCP of this line is peculiar since it does not obey the rules of the NCP mentioned in the previous paragraph, in particular, the NCP is not symmetric with respect to the line dividing the sunspot along a solar radial direction (Schlichenmaier & Collados 2002, Fig. 8, § 4.3). Due to this symmetry breaking, the extreme NCP for Fe I  $\lambda 15648 \text{ \AA}$  does not occur in the penumbral regions closest to the so-

lar limb. This behavior is attributed by Schlichenmaier et al. (2002) and Müller et al. (2002) to the action of Magneto-Optical Effects (MOE) in the radiative transfer. MOE are significant only for very large Zeeman splittings (e.g., Landi Degl’Innocenti & Landi Degl’Innocenti 1973), which is indeed the regime to be applied to the strongly Zeeman sensitive Fe I  $\lambda 15648 \text{ \AA}$  line. Due to the existence gradients of magnetic field azimuth along the line-of-sight, MOE create NCP out of linear polarization signals (Schlichenmaier et al. 2002; Müller et al. 2002). These gradients of azimuth are produced by the existence of two magnetic components in the resolution element having different magnetic field inclination with respect to the vertical. When the line-of-sight is not along the vertical direction, the differences of vertical inclination render differences of azimuth in the plane perpendicular to the line-of-sight. (For a very intuitive representation of the effect, see Fig. 4 in Kàlmàn 1991.) The magnetic geometry required by Schlichenmaier et al. (2002) and Müller et al. (2002) is already present in the model sunspot that we retrieve and, in principle, it has the potential to reproduce the observed Fe I  $\lambda 15648 \text{ \AA}$  NCP. Figure 19 shows the NCP produced by Fe I  $\lambda 15648 \text{ \AA}$  assuming an axi-symmetric sunspot located at  $\mu = 0.7$ . (We have used one randomly chosen model

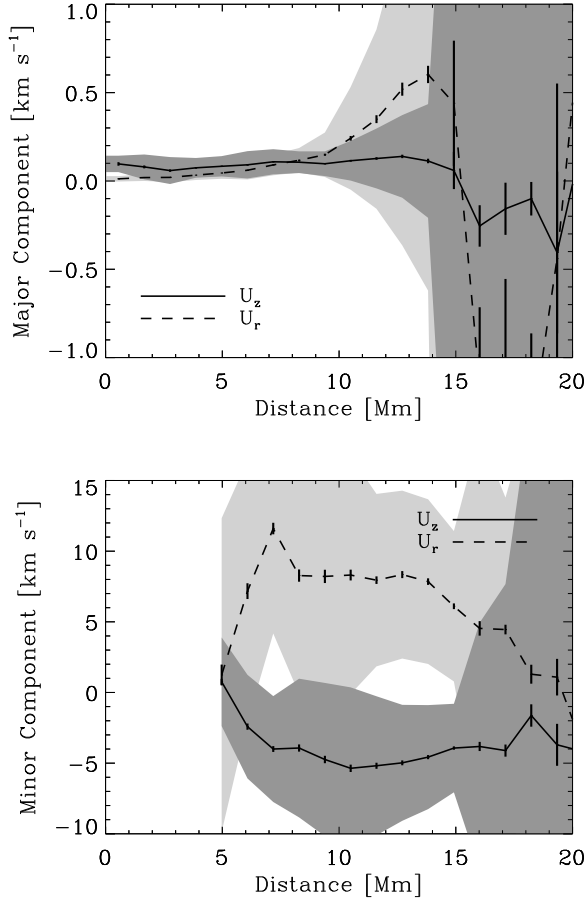


FIG. 16.— Horizontal  $U_r$  and vertical  $U_z$  velocities of the two magnetic components of the model MISMA at  $\log \tau_c = -1$ . We represent the mean (lines) and the standard deviation (shaded regions) for all pixels at a distance from the sunspot center. The major component is in the upper plot whereas the bottom plot corresponds to the minor component. Positive velocities are upward ( $U_z$ ) and outward ( $U_r$ ). The vertical bars correspond to the formal error bars of the mean velocities.

MISMA to represent the thermodynamic state and the velocities in the atmosphere of this axi-symmetric sunspot.) The synthetic Fe I  $\lambda 15648 \text{ \AA}$  NCP turns out to be in good agreement with the observed spatial distribution. Figure 19 also includes the NCP of Fe I  $\lambda 6302.5 \text{ \AA}$ , which is symmetric with respect to the line along the solar radial direction (arrows in Fig. 19).

#### 4.7. Wilson depression

The presence of a strong magnetic field evacuates and cools down the sunspot atmosphere with respect to the non-magnetic quiet Sun. The resulting drop of density produces a depression of the observed sunspot photosphere with respect to the non-magnetic photosphere. Figure 20 shows the depth of the layer  $\tau_c = 1$  as a function of the position in the sunspot (i.e., the Wilson depression). Refer to § 3.5 for the estimate of absolute heights. The Wilson depression of the sunspot core is smaller than the values reported in the literature, even keeping in mind the 100 km uncertainty worked out in Appendix A. For example, *Allen's Astrophysical Quantities* quotes  $(-0.6 \pm 0.2) \text{ Mm}$  (Solanki 2000), whereas we get  $-0.25 \text{ Mm}$  instead (Fig. 20a). Despite the discrepancy, we

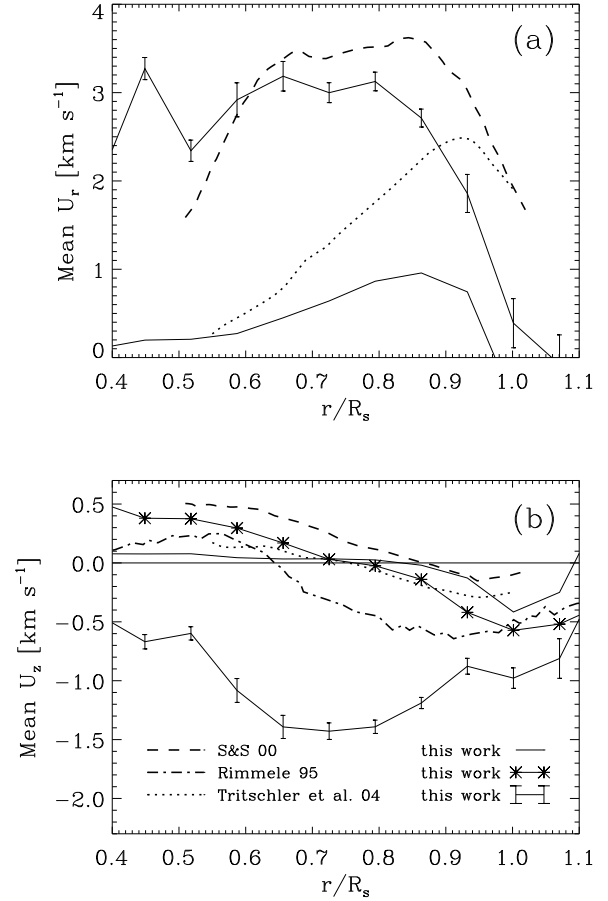


FIG. 17.— Average horizontal (a) and vertical (b) velocities as retrieved from the MISMA inversions. Positive means radially outward (a) and vertically upward (b). The solid lines with error bars show the volume average of the two components, whereas the plain solid lines correspond to the density weighted average. The other lines are shown for reference, and they correspond to works finding downflows within the sunspot boundary (Rimmele 1995, the dotted dashed line; Schlichenmaier & Schmidt 2000, the dashed line, where we only represent one among the four targets; Tritschler et al. 2004, the dotted line). The solid line with asterisks shows the mean vertical velocities we deduce from the bisector of Fe I  $\lambda 6301.5 \text{ \AA}$ , simulating one of the measurements from the literature. The radial distance  $r$  has been referred to the sunspot radius  $R_S$  to allow comparison between sunspots of different radii.

trust our estimate because the semi-empirical model sunspot reproduces the observations on which the large Wilson depressions reported in the literature are based on.

First, there are estimates based on the correlation between magnetic field strength  $B$  and continuum intensity  $I_c$  (e.g., Kopp & Rabin 1992; Martínez Pillet & Vázquez 1993):

$$I_c = \left(1 - \frac{B^2}{4\pi P(W_D)}\right) I_{c0}. \quad (9)$$

The symbol  $P(W_D)$  stands for the gas pressure at the Wilson depression in the non-magnetic Sun, where  $I_c = I_{c0}$ . The relationship (9) is inspired by the condition of magnetostatic equilibrium of an axi-symmetric sunspot (for details, see the papers cited above). The Wilson depression  $W_D$  is determined carrying out a linear regression  $B^2$  versus  $I_c$  that provides a slope  $m$  and a constant  $k$ ,

$$I = mB^2 + k. \quad (10)$$

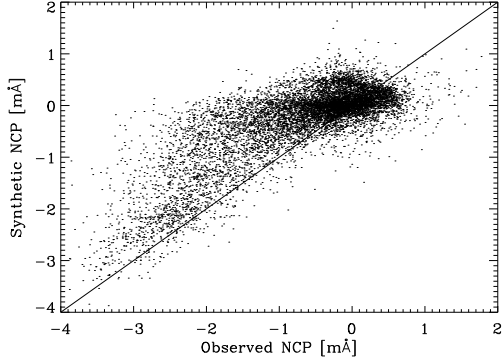


FIG. 18.— Net Circular Polarization (NCP) of Fe I  $\lambda 6302.5$  Å. Scatter plot of synthetic NCP versus observed NCP. The synthetic values slightly underestimate the observed ones (the solid line corresponds to equal synthetic and observed NCPs). However, observations and modeling follow the same tendency and have the same spatial distribution across the sunspot (see main text).

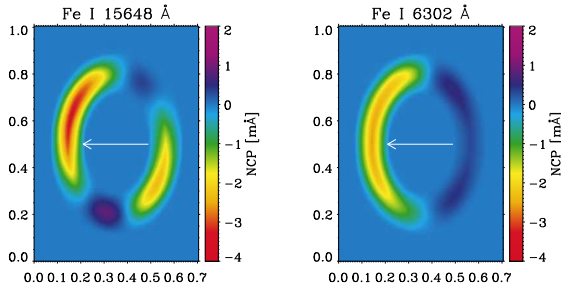


FIG. 19.— Net Circular Polarization (NCP) of Fe I  $\lambda 15648$  Å (left) and Fe I  $\lambda 6302.5$  Å (right) when one of the model MISMA is used to produce an axi-symmetric magnetic field distribution. This axi-symmetric distribution is observed from the side to mimic a sunspot observed at  $\mu = 0.7$ . Note how the NCP of Fe I  $\lambda 6302.5$  Å is almost symmetric with respect to the line along the solar radial direction (indicated by the arrow, whose tip points the solar limb direction). This symmetry disappears for Fe I  $\lambda 15648$  Å, an effect observed by Schlichenmaier & Collados (2002), and explained by Schlichenmaier et al. (2002) and Müller et al. (2002) in terms of a thick horizontal fluxtube embedded in a more vertical magnetic background. Our models also explain this observation. See text for details. The spatial coordinates are given in arbitrary units.

Then, inverting equation (9),

$$W_D = P^{-1} \left[ -k / (4\pi m) \right], \quad (11)$$

where the depth corresponding to a given gas pressure (the inverse  $P$  function or  $P^{-1}$ ) is derived from Spruit (1974) convection zone model. Figure 21 shows the scatter plot between the observed continuum intensity and the mean magnetic field strength provided by the inversion at an optical depth representative of the formation of the spectral lines ( $\log \tau_c = -1$ ). It also shows two linear fits obtained using  $I_c < 0.8$  (the solid line) and  $I_c < 0.5$  (the dashed line). The application of equation (11) renders  $W_D \simeq -0.5$  Mm in both cases. This figure is consistent with the values reported in the literature, but overestimates the true Wilson depression of the model sunspot by a factor two.

Second, most Wilson depression measurements have been

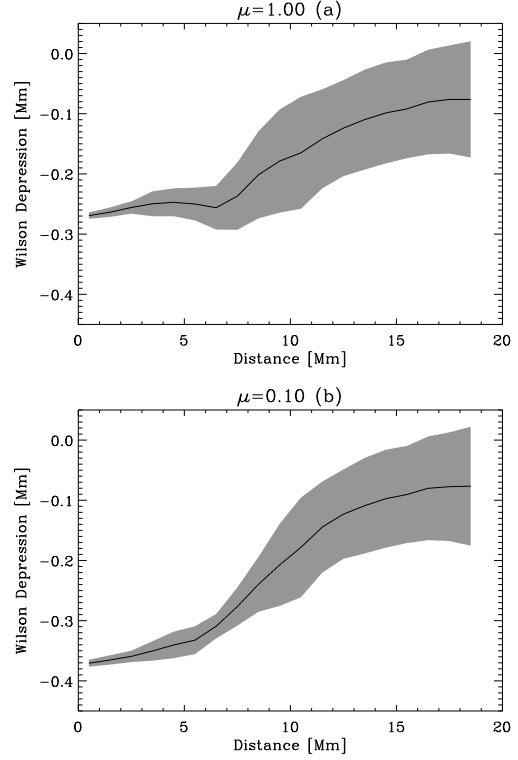


FIG. 20.— Wilson depression as a function of the radial distance within the sunspot. The shaded region corresponds to the standard deviation among those points having the same radial distance from the sunspot center. (a) Wilson depression for the observed sunspot, with  $\mu \simeq 1$ . (b) Wilson depression if the sunspot were close to the solar limb ( $\mu = 0.1$ ). Note how the Wilson depression increases toward the limb.

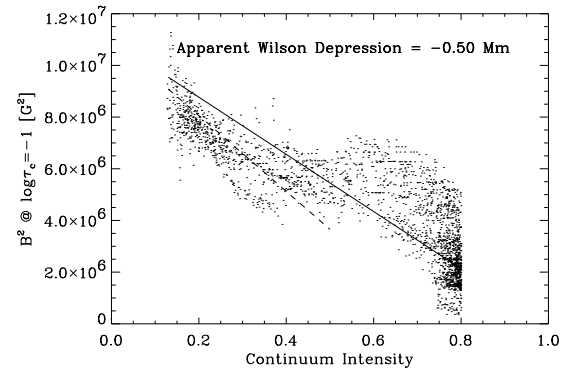


FIG. 21.— Scatter plot of the square of the magnetic field strength  $B^2$  versus continuum intensity. Linear fits of this empirical relationship have been used to estimate the Wilson depression of sunspots at the solar disk center. The two linear regressions consider continuum intensities  $< 0.8$  (the solid line) and continuum intensities  $< 0.5$  (the dashed line). Both provide an apparent Wilson depression of about  $-0.5$  Mm, which overestimates the true Wilson depression of the model sunspot ( $-0.25$  Mm).

carried out for sunspots at the solar limb. Close to the limb the Wilson effect becomes conspicuous, and it allows estimating the depression from simple geometrical arguments. In particular, the center-side penumbra becomes shorter than the limb-side penumbra (e.g., Bray & Loughhead 1974, §3.8). The estimates of the Wilson depression based on this foreshortening also exceed the value that we infer at disk center. However, the Wilson depression of our model sunspot varies with the

position on the disk. It increases toward the solar limb. The physical basis is simple: pressure and density scale heights are proportional to the temperature and, therefore, they are much smaller in the umbra than in the non-magnetic photosphere. Consequently, the range of atmospheric heights contributing to the observed light is narrower in the umbra. The umbral photosphere is not only deeper but thinner. Since limb observations reveal high photospheric layers, the Wilson depression necessarily increases toward the limb. We have estimated the center-to-limb variation of the Wilson depression as follows. For plane parallel atmospheres, the optical depth of an atmospheric layer changes with the position on the disk as

$$\tau_c(\mu) = \tau_c(1)/\mu, \quad (12)$$

with  $\mu$  the cosine of the heliocentric angle  $\theta$ , and  $\tau_c(1)$  the optical depth at disk center. The Wilson depression at  $\mu$  is the height in the atmosphere having  $\tau_c(\mu) = 1$ , which corresponds to the disk center optical depth equals  $\mu$ . In general, the plane parallel approximation is not valid to describe our model sunspot close to the limb, since the photon mean free path becomes larger than the pixel size at the disk center. However, it is a fair approximation to describe the Wilson depression of the umbral core, where the physical properties vary on a scale much larger than the resolution element (e.g., see Fig. 20a). The same approximation is also valid in the quiet Sun, which we have used to set the absolute height of the Wilson depression (§ 3.5). Figure 20b shows the Wilson depression at  $\mu = 0.1$  ( $\theta \simeq 84^\circ$ ) following from equation (12). It turns out to be larger than the depression at the disk center, explicitly, close to  $-0.4$  Mm in the umbral core. Is this value compatible with the observations of the Wilson effect near the limb? It provides a fair description of the most conspicuous property of the Wilson effect, namely, the differential foreshortening of the limb-side penumbra  $d_l$  as referred to the center-side penumbra  $d_c$  (see Fig. 22). Using simple geometrical arguments, it is possible to write down an expression for this foreshortening that depends only on the depression of the umbra  $W_D$  and the radii of the umbra  $R_U$  and the penumbra  $R_S$ ,

$$d_l/d_c = \frac{(R_S - R_U)\mu + W_D\sqrt{1 - \mu^2}}{(R_S - R_U)\mu - W_D\sqrt{1 - \mu^2}}. \quad (13)$$

(Expressions similar to equation [13] are used to infer Wilson depressions from observed foreshortenings, e.g., Chistyakov 1962.) Using equation (13) and the Wilson depressions of the model umbra at various heliocentric angles, we compute the differential foreshortening. It is shown in Fig. 23. The same figure includes values reported in the literature (the square symbols labeled as *observed*; Jensen et al. 1969). The model sunspot follows the observed tendency. The ratio is a little too small, but keep in mind that the observed curve represents mean values, and the individual sunspots do show significant deviations from these mean values (see., e.g., the points in Fig. 6 of Jensen et al. 1969). If one fits the foreshortening observed at the limb using as a constant free parameter  $W_D$  in equation (13),  $W_D \simeq -0.45$  Mm (see the dashed line in Fig. 23). This value is close to that in Fig. 20b, which allows us to argue that the low Wilson depression of our model sunspot at  $\mu = 1$  is consistent with the Wilson depressions reported for sunspots at the limb ( $\mu \ll 1$ ).

Note yet another property of the Wilson depression in our model sunspot. The outer penumbra is depressed with re-

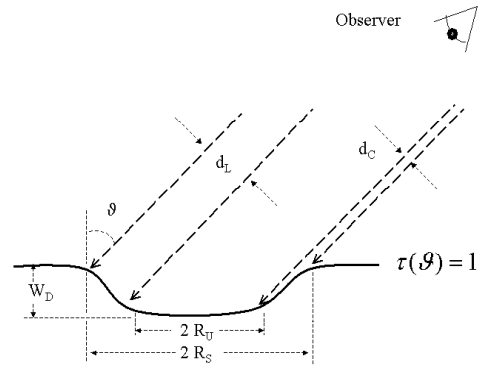


FIG. 22.— Schematic of a sunspot observed away from the solar disk center. The solid line represents the height in the atmosphere where the continuum optical depth equals one at the heliocentric angle of observation  $\theta$ . The figure also shows various symbols used to describe the Wilson effect of our model sunspot, in particular, the different foreshortening of the limb-side penumbra  $d_l$  and the center-side penumbra  $d_c$ .

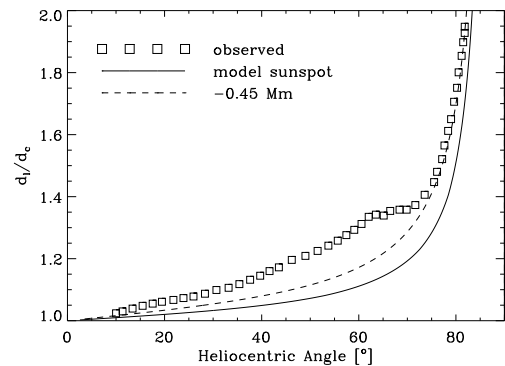


FIG. 23.— Ratio between the size of the limb-side penumbra  $d_l$  and the center-side penumbra  $d_c$  versus heliocentric angle of the sunspot. The crude estimate from our model sunspot (the solid line) provides a fair description of the mean observation (the symbols). The dashed line is a best fit description of the observations at the limb, and it yields a Wilson depression of  $-0.45$  Mm. Heliocentric angles are given in degrees.

spect to the quiet photosphere by about 100 km. The curves in Fig. 20 do not show a sharp transition at the penumbral boundary (distance  $\sim 17$  Mm) because they represent the Wilson depression of the magnetized fraction of the atmosphere. However, outside the penumbral border the stray light contamination of the model atmospheres occupies most of the resolution elements, and the Wilson depression of this stray light is basically zero. Consequently, there is a significant discontinuity of the observed layers at the penumbral border, which is bound to complicate the interpretation of all observables.

To sum up, the model sunspot obtained from the inversion provides large apparent Wilson depressions consistent with those reported in the literature, despite the fact that the true Wilson depression is rather small. In addition, there is a significant discontinuity of the depression at the penumbral border.

## 5. MAGNETIC FLUX CONSERVATION

One can reproduce the asymmetries of the Stokes profiles observed in sunspots assuming that the magnetic field varies monotonically with height (Sánchez Almeida & Lites

1992; Westendorp Plaza et al. 2001; Mathew et al. 2003). It requires atmospheres having vertical gradients of magnetic field inclination. However, the gradients are too large to fit in the global topology of the sunspot magnetic field (Sánchez Almeida & Lites 1992). Solanki et al. (1993) formulate the problem pointing out that the divergence of the resulting magnetic field differs from zero and, consequently, the magnetic flux is not conserved. A way out was proposed by Solanki & Montavon (1993). The gradient of magnetic field inclination does not have to be monotonic. A horizontal magnetic field embedded in a more inclined background field also provides the observed Stokes asymmetries. Solanki & Montavon (1993) use a single thick horizontal fluxtube to explain the idea, but a collection of thin fluxtubes does the same effect. The latter is actually the MISMA model proposed by Sánchez Almeida et al. (1996), and the approach followed in this paper (§ 3.1). Since the conservation of magnetic flux is central to assess the consistency of the retrieved model atmospheres, we have checked it with care. We use the differential formulation  $\nabla \mathbf{B} = 0$ , with  $\mathbf{B}$  the magnetic field vector.

The inversions do not provide details on the micro-structure that give rise to the asymmetries. They are optically-thin and the spectra are only sensitive to mean quantities (Sánchez Almeida et al. 1996). However, the condition  $\nabla \mathbf{B} = 0$  is also satisfied by the volume-averaged magnetic field, since integration and derivation are linear operators and commute (Sánchez Almeida 1998). Specifically,

$$\nabla \langle \mathbf{B} \rangle = 0, \quad (14)$$

where the angle brackets  $\langle \rangle$  are employed as in previous sections to represent volume average. These volume averages are precisely the quantities provided by the MISMA IC (Sánchez Almeida 1997). In order to carry out tests, we employ equation (14) integrated azimuthally. Using cylindrical coordinates, equation (14) becomes

$$\frac{\partial}{\partial z} \langle B_z \rangle + \frac{1}{r} \frac{\partial}{\partial r} (r \langle B_r \rangle) = 0, \quad (15)$$

with  $B_z$  and  $B_r$  the vertical and radial components of the magnetic field, and with the hat-symbol meaning azimuthal average,

$$\langle B_z \rangle = \frac{1}{2\pi} \int_0^{2\pi} \langle B_z \rangle d\chi. \quad (16)$$

Figure 24a shows the two terms of equation (15). We compute the gradients at equal continuum optical depths ( $\log \tau_c = -1$ ). Ideally, one should estimate horizontal gradients using magnetic fields at a fixed geometrical height. However, we do it at constant optical depth keeping in mind that  $\nabla \langle \mathbf{B} \rangle = 0$  must hold locally and that the pixel-to-pixel variation of the Wilson depression is negligible (see Appendix A). Our approach has the advantage of avoiding the noise introduced when setting a common scale of heights. The sign of the vertical gradient has been switched in Fig. 24 so that the magnetic flux is conserved when the two curves are identical. The two terms are indeed equal within a fraction of  $\text{G km}^{-1}$ . For the sake of comparison, Fig. 24b also shows the same two terms corresponding to an inversion where the asymmetries are obtained by monotonic variation of the magnetic field inclination along the line-of-sight. We derive the horizontal and vertical gradients from Fig. 9 of Westendorp Plaza et al. (2001). The vertical gradients are computed using the magnetic field strengths and inclinations at two extreme optical depths ( $\log \tau_c = 0$

and assuming  $d\tau_c/dz = -140 \text{ km}$ . The horizontal gradients are computed from the field strength and the inclination at  $\log \tau_c = -1.5$ . Figure 24c shows another inversion that reproduces the Stokes asymmetries of Fe I  $\lambda 15648 \text{ \AA}$  resorting to monotonic variations of magnetic field inclination along the line-of-sight. We use Fig. 15 of Mathew et al. (2003), and the above  $d\tau_c/dz$ . The MISMA inversion fulfills the condition of magnetic flux conservation in the penumbra better than the others. For the penumbral points, the mean absolute values of the residuals are,

$$|\nabla \langle \mathbf{B} \rangle| \sim \begin{cases} 0.2 \text{ G km}^{-1} & \text{this work,} \\ 1.2 \text{ G km}^{-1} & \text{SIR,} \\ 4.3 \text{ G km}^{-1} & \text{SPINOR,} \end{cases} \quad (17)$$

where SIR and SPINOR refer to the name of the IC employed by Westendorp Plaza et al. (2001) and Mathew et al. (2003), respectively.

The reason why MISMA inversions conform with the magnetic flux conservation is simple. The gradients of magnetic field inclination required to reproduce the Stokes  $V$  asymmetries are provided by the micro-structure, rather than from systematic variations of  $\langle B_z \rangle$ . There is no way two separate small and large spatial scales when only smooth gradients along the line-of-sight are permitted. Exactly for this reason, the same self-consistency found for MISMA is expected in other inversions that allow for unresolved structure, even though it may not necessarily be optically-thin (e.g., those with a single fluxtube embedded in more vertical background; Bellot Rubio 2004; Borrero et al. 2004)

## 6. MASS CONSERVATION

We have all the physical variables required to test the model sunspot for consistency with mass conservation. The issue of mass conservation, in particular at the penumbral boundary, has been traditionally regarded as one of the difficulties-troubles-mysteries of the Evershed effect (e.g. Thomas 1994). Figure 25 shows the mass per unit time and surface traveling upward ( $\alpha \rho U_z$ ; Fig. 25a) and outward ( $\alpha \rho U_r$ ; Fig. 25b). It includes the two MISMA components separately, as well as net mass flux carried together. First, note that the large velocities of the minor component actually transport little mass, i.e., similar to the mass transported by the very modest velocities of the major component. This moderate mass flow results from the very low density of the minor component (Fig. 14) and, to a less extent, to its reduced OCF (Fig. 8). The mean mass transported upward by the major component is roughly balanced by the mean mass transported downward by the minor component. Figure 25b shows the horizontal mass flow. It is positive for both the minor and the major components, meaning that it is directed outward. This horizontal flow decreases to zero at the penumbral boundary (see the dotted line in Fig. 25b at a distance of 16 Mm). Is the mass disappearing? The horizontal mass flux seems to turn into downflows at the penumbral boundary. Note how the vertical mass flow becomes negative at the external edge (the dotted line in Fig. 25a at 16 Mm). More specifically, the upflows associated with the major component turns to zero so that only the minor component downflows remain (the dashed line in Fig. 25a). According to this picture, at the penumbral boundary the major components cease to carry mass. We just see a return mass flow similar to that existing in the rest of the penumbra. Formal errors for the mean net mass flows are included in Fig. 25. They are computed following the recipe in § 4.3 and § 4.5. As we point out in § 4.7, the Wilson depression changes abruptly at

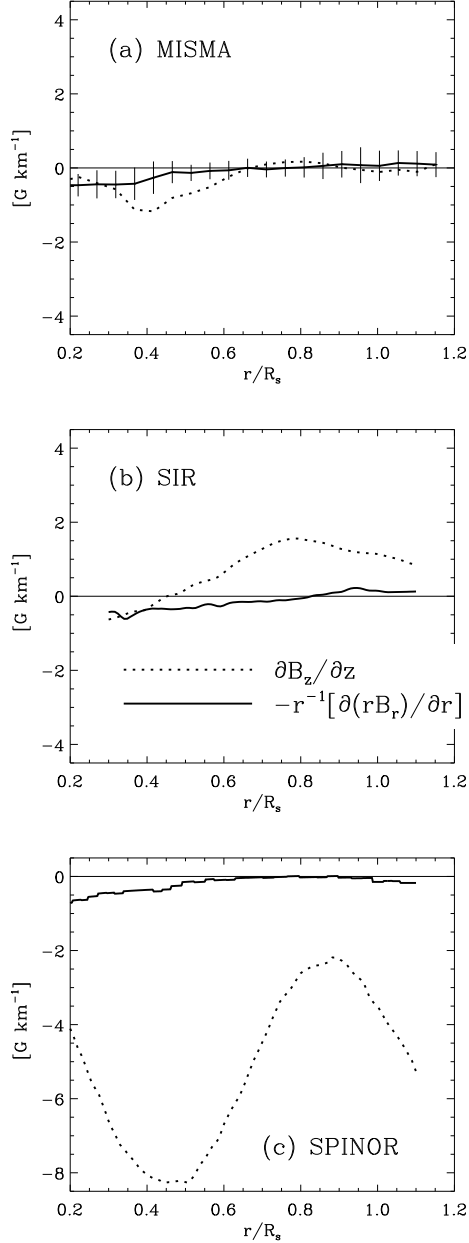


FIG. 24.— (a) Horizontal and vertical gradients of the horizontal and vertical components of the retrieved magnetic field vector. The solid and dotted lines represent the horizontal and the vertical gradients, as indicated by the inset in (b). The error bars show the standard deviation of the gradients among all points at a radial distance from the sunspot center ( $r/R_S$ , with  $R_S$  the sunspot radius). For the divergence of the magnetic field to be zero, the two curves should be equal. The top panel shows the curves resulting from our inversion. For comparison, the panel (b) contains the inversion by Westendorp Plaza et al. (2001), where gradients occur only along the line-of-sight. Panel (c) shows the inversion by Mathew et al. (2003), which have been carried out under the same assumption. Except for a shift, the ordinates of the three plots are identical.

the penumbral border. This caveat must be considered when pursuing the Evershed flow outside the sunspot.

#### 7. THE ROLE OF THE MINOR COMPONENT IN THE RADIATIVE TRANSFER

The minor component is able to modify the spectral line shapes, despite the fact that it carries a minute fraction of

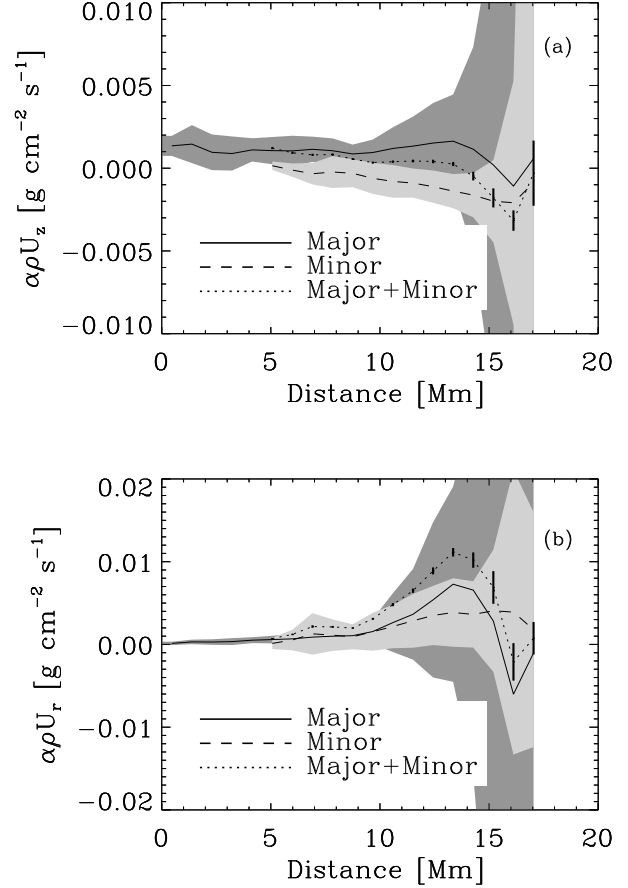


FIG. 25.— Mass flows in the vertical direction (a; positive upward) and in the horizontal direction (b; positive outward). Despite they have very different velocities, major and minor components transport similar amounts of mass. Note that there is no net vertical mass flow, except at the penumbral border (a; the dotted line). The shaded areas represent the standard deviation of the minor and major mass flows. The vertical bars represent the formal error bars of the Minor+Major mean curves (the dotted lines).

the major component mass (about 5%; § 4.5). This apparent contradiction admits a reasonable explanation. Whenever the minor component contends with the major component to modify a line shape, it loses. This is the reason why the minor component cannot modify the cores of the lines, whose absorption is provided by the major component. However, due to the Doppler shift produced by the large velocities of the minor component, it often absorbs in the wings of the major component absorption, where the contribution of the major component is not so overwhelmingly dominant. Thus the minor component can change the line wings, producing line asymmetries from which we infer its presence. Figure 26 tries to illustrate this simple explanation showing how the Stokes  $I$  bisector is modified by the velocity of the minor component. The figure shows a Fe I  $\lambda 6302.5$  Å Stokes  $I$  synthetic profile corresponding to a point in the limb-side penumbra. It also includes the bisector, i.e., a line joining the mid points of the profile at each intensity level. The shift of the bisector is often used to measure velocities (e.g., § 4.5). Figure 26b shows various synthetic bisectors obtained with the same model MISMA when the minor component velocity is varied

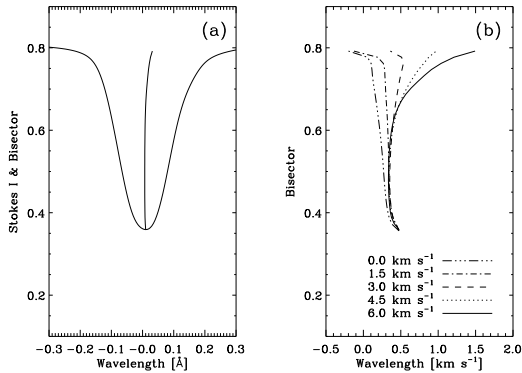


FIG. 26.— (a) Stokes  $I$  profile and its bisector for a typical point in the limb-side penumbra. (b) Bisectors corresponding to the model MISMA in (a) when the velocities of the minor component are modified according to the legend in the figure. Note how the line core is insensitive to the minor component speed. However, the speed of the minor component produces significant modifications of the bisector at the line wings.

from zero to the value retrieved from the inversion<sup>8</sup>. Note how the bisector position at the line core is basically insensitive to the minor component velocity. However, in the line wings the bisector traces the minor component velocity with a measurable amplitude ( $2 \text{ km s}^{-1}$ ).

## 8. CONCLUSIONS

Magnetic atmospheres having optically-thin micro-structure account for the line polarization observed in plage, network and internetwork regions (see the references in § 1). This kind of atmosphere is called Micro-Structured Magnetic Atmosphere or MISMA. Our paper shows how MISMA also account for the Stokes profiles of sunspots, including the cross-over effect (§ 3.3).

We have carried out a systematic fit of 10130 Stokes  $I$ ,  $Q$ ,  $U$  and  $V$  profiles of Fe I  $\lambda 6301.5 \text{ \AA}$  and Fe I  $\lambda 6302.5 \text{ \AA}$ . They correspond to the polarization emerging from a field-of-view containing a round sunspot (Fig. 1). The fits (also called inversions) provide a model MISMA per pixel. Each model MISMA has two magnetic components with different magnetic fields and mass flows interleaved along the line-of-sight<sup>9</sup> (§ 3.1). Due to the nature of the radiative transfer through a system of optically-thin micro-structures, such simplified model MISMA only provide the mean properties of the solar atmosphere. In particular, we are not sensitive to the size of the individual micro-structures forming each component (but the micro-structures are optically-thin and so thinner than say 100 km). By assembling the results of all 10130 inversions, we set up a model sunspot with micro-structure. Its mean magnetic field and mass flow is in good agreement with the standard sunspot magnetic field topology. The vertical magnetic fields of the umbra fan out and render almost horizontal fields at the external penumbral border. Quasi horizontal mass flows of a few  $\text{km s}^{-1}$  exist throughout the penumbra.

This regular large scale behavior coexists with an unexpected micro-structure. We need to distinguish between the

<sup>8</sup> Of the order of  $6 \text{ km s}^{-1}$  in the layers where the line is formed.

<sup>9</sup> The fact that this MISMA scenario is so close to the scenarios employed for plage, network and inter-network regions reflects the degeneracy of the radiative transfer for MISMA (Sánchez Almeida et al. 1996). The use of only two components is an idealization that we imposed, and it actually shows the need for more than one component to account for the observed line shapes.

minor and the major magnetic components in each resolution element. The major component is the one having most of the mass. This terminology allows us to describe the micro-structure of the magnetic fields and the mass flows as follows;

1. The magnetic fields of the minor and the major components have very different inclinations, with the major component being more vertical than the minor component. Actually, the field lines of the minor component bend over to return to the sub-photosphere. This return of magnetic field lines occurs over the entire penumbra, rather than at the outer penumbra (§ 4.2; Fig. 9a).
2. By construction, the magnetic field lines and mass flows are always parallel. Consequently, the minor component carries downflows. According to our inversions, both upflows and downflows are present everywhere on the penumbra. The velocities along field lines are small for the major component (several hundred  $\text{m s}^{-1}$ ), and large for the minor component ( $10 \text{ km s}^{-1}$ ; see Fig. 16).
3. At equal optical depths, the major component has mass densities similar to the unmagnetized photosphere. The densities of the minor component are five times smaller (§ 4.4).
4. The minor component occupies a small fraction of the atmosphere (about 30% of the penumbra, to become absent in the umbra; § 4.1 and Fig. 8).
5. Despite the large difference of velocity, the flows of the major and the minor components transport very similar masses (§ 6). In particular, there is almost no vertical transport of mass since the mass involved in upflows and downflows tends to be balanced.
6. The minor component has magnetic field strengths 10% larger than the major component. If connected by field lines, the resulting difference of magnetic pressure can lead to a siphon flow from the major component to the minor component whose magnitude is similar to the observed Evershed flow (§ 4.3).
7. A sizeable fraction of the unsigned magnetic flux emerging in the penumbra returns to the photosphere in situ. In the external penumbral rim, the vertical magnetic flux is only a small fraction of the unsigned flux (only 20%). This result produces a considerable difference between the signed and unsigned magnetic fluxes of the sunspot (§ 4.3).
8. The model sunspot has a Wilson depression of  $-0.25 \text{ Mm}$  at the solar disk center, and it significantly increases toward the limb (§ 4.7).

Counter-intuitive as it may sound, the presence of field lines pointing up and down over the entire penumbra does not obviously conflict with existing observations. We have carried out several tests to check the internal consistency of the retrieved model sunspot.

- The MISMA inversions account for the asymmetries of the Stokes profiles with a magnetic field vector  $\mathbf{B}$  which does not violate the  $\nabla \mathbf{B} = 0$  condition (§ 5).

- Although, the model sunspot has a Wilson depression smaller than the typical values found in the literature, it reproduces the observables from which large Wilson depressions are inferred (§ 4.7).
- The model sunspot reproduces the Net Circular Polarization (NCP) of the observed lines, including their rules. In addition, it also reproduces the abnormal behavior of the NCP of Fe I  $\lambda 15648$  Å, discovered and explained by Schlichenmaier and co-workers using magnetic structures larger than the ones implicit in the MISMA assumption (§ 4.6).
- When the observed Stokes profiles are interpreted assuming a single magnetic component per resolution element, one finds upflows in the inner penumbra and downflows in the outer penumbra (§ 4.5; Fig. 17). These upflows and downflows appear in the recent penumbral literature. According to our interpretation, they are artificially produced when the unresolved structure of the flows is neglected (§ 4.5). It would be similar to the well known convective blueshift of the non-magnetic granulation, which does not correspond to a true systematic motion.
- Despite of the partial cancellation of vertical magnetic flux in the penumbra, some net magnetic flux remains. The existence of such residual flux avoids an obvious disagreement of the model sunspot with existing observations. Chromospheric and coronal images often show fieldlines connecting the penumbra with magnetic structures far away from the sunspot (see, e.g., Weiss et al. 2004).
- The minor component contributes to the emerging spectrum despite the fact that they contain a minute fraction of the total penumbral mass (5% or less). Such a disproportionate effect results from the large Doppler shifts associated with the minor components, which absorb in

the wings of the major component absorption profiles (§ 7).

The interpretation of all these results in the context of a coherent sunspot magnetic structure is deferred for a separate paper (Sánchez Almeida 2005). We prefer to disconnect the fact that MISMA accounts for the Stokes asymmetries observed in sunspots (this work), from the more speculative physical interpretation of the retrieved micro-structure. Even if the physical interpretation is eventually shown to be wrong, MISMA would still account for the asymmetries. Only one general remark concerning the global magnetic structure will be made. The mass flows and magnetic fluxes of the minor and major components are surprisingly similar. This suggests a physical connection between them, so that field lines and flows emerging as the major component return to the photosphere as the minor component of the same or a neighbor resolution element. This possibility is not a direct result of the MISMA inversion, and it is put forward as a mere conjecture.

The picture that emerges from our sunspot inversions is in qualitative agreement with the original MISMA scenario for penumbrae put forward by Sánchez Almeida et al. (1996, § 3.1)

A final caveat is in order. The fact that our model sunspot reproduces the observed Stokes asymmetries does not guarantee the accuracy of the model. However, that fact that a model sunspot reproduces the asymmetries should not be undervalued. If the model sunspot that accounts for real sunspots is eventually discovered, it will be found among those in this rare category of models reproducing the Stokes asymmetries.

Special thanks are due to B. Lites and J. Thomas, who supplied the data analyzed in this work and provided insightful comments on an earlier version of the manuscript. The work has partly been funded by the Spanish Ministry of Science and Technology, project AYA2001-1649, as well as by the EC contract HPRN-CT-2002-00313.

#### REFERENCES

- Beckers, J. M. 1977, *ApJ*, 213, 900  
 Bellot Rubio, L. R. 2004, *Rev. Mod. Astron.*, 17, 21  
 Bellot Rubio, L. R., Balthasar, H., Collados, M., & Schlichenmaier, R. 2003, *A&A*, 403, L47  
 Borrero, J. M., Lagg, A., Solanki, S. K., & Collados, M. 2004, *A&A*, submitted  
 Bray, R. J., & Loughhead, R. E. 1974, *Sunspots* (New York: Dover)  
 Bumba, V. 1960, *Izv. Crim. Astrophys. Obs.*, 23, 253  
 Chistyakov, V. F. 1962, *Soviet Astronomy*, 6, 363  
 del Toro Iniesta, J. C., Bellot Rubio, L. R., & Collados, M. 2001, *ApJ*, 549, L139  
 Dravins, D. 1982, *ARA&A*, 20, 61  
 Elmore, D. F., Lites, B. W., Tomczyk, S., Skumanich, A., Dunn, R. B., Schuenke, J. A., Streaender, K. V., Leach, T. W., Chambellan, C. W., Hull, H. K., & Lacey, L. B. 1992, *Proc. SPIE*, 1746, 22  
 Golovko, A. A. 1974, *Sol. Phys.*, 37, 113  
 Grigorjev, V. M., & Katz, J. M. 1972, *Sol. Phys.*, 22, 119  
 Illing, R. M. E., Landman, D. A., & Mickey, D. L. 1974a, *A&A*, 35, 327  
 —. 1974b, *A&A*, 37, 97  
 Jensen, E., Brahde, R., & Ofstad, P. 1969, *Sol. Phys.*, 9, 397  
 Kålmån, B. 1991, *Sol. Phys.*, 135, 299  
 Kopp, G., & Rabin, D. 1992, *Sol. Phys.*, 141, 253  
 Landi Degl'Innocenti, E. 1992, in *Solar Observations: Techniques and Interpretation*, ed. F. Sánchez, M. Collados, & M. Vázquez (Cambridge: Cambridge University Press), 71  
 Landi Degl'Innocenti, E., & Landi Degl'Innocenti, M. 1973, *Sol. Phys.*, 31, 299  
 Lites, B. W., Elmore, D. F., Seagraves, P., & Skumanich, A. 1993, *ApJ*, 418, 928  
 Lites, B. W., Thomas, J. H., Bogdan, T. J., & Cally, P. S. 1998, *ApJ*, 497, 464  
 Müller, D. A. N., Schlichenmaier, R., Steiner, O., & Stix, M. 2002, *A&A*, 393, 305  
 Makita, M. 1986, *Sol. Phys.*, 106, 269  
 Martínez Pillet, V., Lites, B. W., & Skumanich, A. 1997, *ApJ*, 474, 810  
 Martínez Pillet, V., & Vázquez, M. 1993, *A&A*, 270, 494  
 Mathew, S. K., Lagg, A., Solanki, S. K., Collados, M., Borrero, J. M., Berdyugina, S., Krupp, N., Woch, J., & Frutiger, C. 2003, *A&A*, 410, 695  
 Meyer, F., & Schmidt, H. U. 1968, *Mitteilungen der Astronomischen Gesellschaft Hamburg*, 25, 194  
 Priest, E. R. 1982, *Solar Magneto-hydrodynamics* (Dordrecht: Reidel)  
 Rüedi, I., Solanki, S. K., & Keller, C. U. 1999, *A&A*, 348, L37  
 Rimmele, T. R. 1995, *ApJ*, 445, 511  
 Sánchez Almeida, J. 2001, in *ASP Conf. Ser.*, Vol. 248, *Magnetic Fields Across the Hertzsprung-Russell Diagram*, ed. G. Mathys, S. K. Solanki, & D. T. Wickramasinghe (San Francisco: ASP), 55  
 Sánchez Almeida, J. 1997, *ApJ*, 491, 993  
 —. 1998, *ApJ*, 497, 967  
 —. 2005, *ApJ*, in preparation  
 Sánchez Almeida, J., Landi Degl'Innocenti, E., Martínez Pillet, V., & Lites, B. W. 1996, *ApJ*, 466, 537  
 Sánchez Almeida, J., & Lites, B. W. 1992, *ApJ*, 398, 359  
 —. 2000, *ApJ*, 532, 1215  
 Scharmer, G. B., Gudiksen, B. V., Kiselman, D., Löfdahl, M. G., & van der Voort, L. H. M. R. 2002, *Nature*, 420, 151  
 Schlichenmaier, R., & Collados, M. 2002, *A&A*, 381, 668  
 Schlichenmaier, R., Müller, D. A. N., Steiner, O., & Stix, M. 2002, *A&A*, 381, L77  
 Schlichenmaier, R., & Schmidt, W. 2000, *A&A*, 358, 1122  
 Skumanich, A., Lites, B. W., Martínez Pillet, V., & Seagraves, P. 1997, *ApJS*, 110, 357  
 Socas-Navarro, H., & Sánchez Almeida, J. 2002, *ApJ*, 565, 1323  
 Solanki, S. K. 1986, *A&A*, 168, 311  
 —. 2000, in *Allen's Astrophysical Quantities - 4th edition*, ed. A. N. Cox (New York: AIP), 367

- Solanki, S. K., & Montavon, C. A. P. 1993, *A&A*, 275, 283  
 Solanki, S. K., & Schmidt, H. U. 1993, *A&A*, 267, 287  
 Solanki, S. K., Walther, U., & Livingston, W. 1993, *A&A*, 277, 639  
 Spiegel, E. A. 1957, *ApJ*, 126, 202  
 Spruit, H. C. 1974, *Sol. Phys.*, 34, 277  
 —, 1981, *A&A*, 98, 155  
 Stellmacher, G., & Wiehr, E. 1971, *Sol. Phys.*, 17, 21  
 Stenflo, J. O., Harvey, J. W., Brault, J. W., & Solanki, S. K. 1984, *A&A*, 131, 333  
 Stix, M. 1991, *The Sun* (Berlin: Springer-Verlag)  
 Thomas, J. H. 1994, in *Solar Surface Magnetism*, ed. R. J. Rutten & C. J. Schrijver, NATO ASI Ser. 433 (Dordrecht: Kluwer), 219  
 Thomas, J. H., & Montesinos, B. 1993, *ApJ*, 407, 398  
 Tritschler, A., Schlichenmaier, R., Bellot Rubio, L. R., & the KAOS Team. 2004, *A&A*, 415, 717  
 Unno, W. 1956, *PASJ*, 8, 108  
 Weiss, N. O., Thomas, J. H., Brummell, N. H., & Tobias, S. M. 2004, *ApJ*, 600, 1073  
 Westendorp Plaza, C., del Toro Iniesta, J. C., Ruiz Cobo, B., Martínez Pillet, V., Lites, B. W., & Skumanich, A. 1997, *Nature*, 389, 47  
 —, 2001, *ApJ*, 547, 1130  
 Wiehr, E. 1995, *A&A*, 298, L17

## APPENDIX

## ERROR OF THE ABSOLUTE SCALE OF HEIGHTS

An absolute scale of heights is derived assuming no variation of the total pressure between adjacent pixels (§ 3.5). The purpose of this appendix is to estimate the error introduced by such assumption.

The true total pressure  $P$  depends not only on the height in the atmosphere,  $z$ , but also on the horizontal coordinates. For the sake of simplicity, we consider an axi-symmetric sunspot so that the horizontal coordinates are reduced to the distance to the sunspot center  $r$ . Let us use  $\tilde{P}(r, z)$  to denote the distribution of pressures inferred assuming that there is no spatial variation of  $P(r, z)$ . The estimated pressures are identical to the true pressures except for a shift of the vertical scale,

$$\tilde{P}(r, z) = P(r, z - z_0(r)). \quad (\text{A1})$$

This shift,  $z_0(r)$ , is the error of the vertical scale that we want to estimate. The  $\tilde{P}(r, z)$  has been constructed so that its variation with the horizontal position is minimum, i.e.,

$$\frac{d\tilde{P}(r, z)}{dr} = \frac{\partial P(r, z - z_0(r))}{\partial r} - \frac{\partial P(r, z - z_0(r))}{\partial z} \frac{dz_0(r)}{dr} \simeq 0. \quad (\text{A2})$$

This expression provides an ordinary differential equation for the error,

$$\frac{dz_0(r)}{dr} \simeq \frac{\partial \ln P(r, z - z_0(r)) / \partial r}{\partial \ln P(r, z - z_0(r)) / \partial z}, \quad (\text{A3})$$

which can be integrated to evaluate  $z_0$ . The right-hand-side of the previous equation can be estimated from the magnetostatic equilibrium equation. It couples the spatial gradients of gas pressure  $P_g$ , radial magnetic field  $B_r$ , and vertical magnetic field  $B_z$  (e.g., Priest 1982, §8.4),

$$\frac{\partial P_g}{\partial r} = \frac{B_z}{4\pi} \left( \frac{\partial B_r}{\partial z} - \frac{\partial B_z}{\partial r} \right). \quad (\text{A4})$$

Using the conservation of magnetic flux in an axi-symmetric sunspot with radial magnetic fields,

$$\frac{\partial B_z}{\partial z} + \frac{1}{r} \frac{\partial(rB_r)}{\partial r} = 0, \quad (\text{A5})$$

and the definition of total pressure,

$$P = P_g + \frac{B_r^2}{8\pi} + \frac{B_z^2}{8\pi}, \quad (\text{A6})$$

it is possible to transform equation (A4) into

$$\frac{\partial P}{\partial r} = -\frac{B_r^2}{4\pi r} + \frac{B^2}{4\pi} \frac{\partial \iota}{\partial z}, \quad (\text{A7})$$

where  $\iota$  stands for the magnetic field inclination with respect to the vertical direction (Fig. 10). (Note that we drop from the expressions the dependence of the physical variables on height and radial position. We do it for the sake of simplicity, without compromising clarity.) The second term of the right-hand-side of equation (A7) vanishes for the kind of atmosphere that we deal with (whose mean vertical gradient of inclination is zero), therefore,

$$\frac{\partial \ln P}{\partial r} \simeq -\frac{2}{1+\beta} \frac{\sin^2 \iota}{r}, \quad (\text{A8})$$

where we use  $\beta$  for the ratio of gas pressure to magnetic pressure,  $\beta = 8\pi P_g / B^2$ . Using this equation plus the definition of the total pressure scale height  $H_P$ ,

$$\frac{\partial \ln P}{\partial z} \equiv -H_P^{-1}, \quad (\text{A9})$$

one can find a very compact expression for the horizontal gradient of the error,

$$\frac{dz_0(r)}{dr} \simeq \frac{2H_P}{1+\beta} \frac{\sin^2 \iota}{r}. \quad (\text{A10})$$

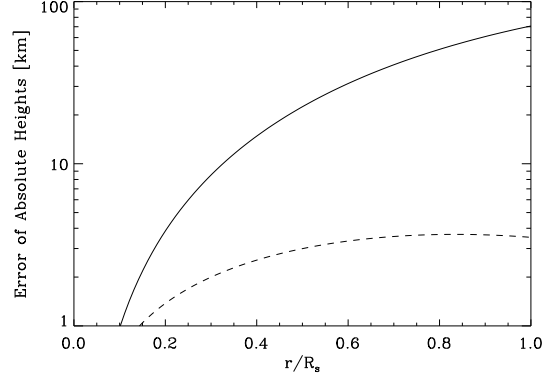


FIG. A27.— Error of the absolute vertical scale due to the assumption that the total pressure does not vary between neighbor pixels. They are represented for each radial position along the sunspot ( $r/R_S$ , with  $R_S$  the sunspot radius). The solid line is the error relative to the sunspot center, whereas the dashed line correspond to the error between two adjacent pixels. Heights are given in km.

This differential equation can be easily used to estimate both, the error between adjacent pixels separated by  $\delta r$ ,

$$\delta z_0(r) \simeq \delta r \frac{dz_0(r)}{dr}, \quad (\text{A11})$$

and the total error from the sunspot center to a given radial distance  $r$ ,

$$\Delta z_0(r) = \int_0^r \frac{dz_0(r')}{dr} dr'. \quad (\text{A12})$$

Figure A27 shows both  $\delta z_0$  and  $\Delta z_0$  computed according to equations (A10), (A11), and (A12), under the assumption  $\beta = 1$ ,  $H_p = 100$  km,  $\delta r \simeq 0.75''$ , and

$$\iota = 80^\circ \frac{r}{R_S}, \quad (\text{A13})$$

with  $R_S$  the sunspot radius. Equation (A13) roughly describes the mean inclination of a sunspot magnetic field (e.g., Solanki 2000, or Fig. 9). The rest of parameters are typical of our penumbral inversions. Note that  $\sin^2 \iota / r \propto r$  in the umbra, so that integrand of equation (A12) is only significant in the penumbra. According to Fig. A27, the pixel-to-pixel error is negligible (smaller than 4 km). The variation across the full spot is larger, but it does not reach 100 km.